Consistent Immersed Volumetric Nitsche Methods for Composite Analysis

Jiarui Wang^a, Guohua Zhou^a, Michael Hillman^{*a}, Anna Madra^a, Yuri Bazilevs^b, Jing Du^c and Kangning Su^c

^a Department of Civil and Environmental Engineering, The Pennsylvania State University, University Park, PA 16802, USA.

^b School of Engineering, Brown University, Providence, RI 02912, USA.

Highlights

- Symmetric and non-symmetric volumetric immersed Nitsche methods proposed
- The proposed weak forms attest to the composite strong form
- Non-conforming discretizations are admissible for background and foreground domains
- Explicit definition of interfaces is not required

Note

This is a pre-print of an article published in Computer Methods in Applied Mechanics and Engineering.

Abstract

Generating quality body-fitting meshes for complex composite microstructures is a non-trivial task. In particular, micro-CT images of composites can contain numerous irregularly-shaped inclusions. Among the methods available, immersed boundary methods that discretize bodies independently provide potential for tackling these types of problems since a matching discretization is not needed. However, these techniques still entail the explicit parameterization of the interfaces, which may be considerable in number. In this work, immersed volumetric Nitsche methods are developed in order to avoid the difficulty of generating body fitting meshes for composite materials with complicated microstructures, and overcome the issues in the surface-type methods. These approaches are developed using Nitsche's techniques to enforce volumetric continuity between the inclusion and background domains. It is shown that the proposed weak forms are fully consistent with the strong form of the composite problem. The present approach permits C^0 approximations for the foreground discretization, and C^1 approximations for the background. The effectiveness of these methods is demonstrated by solving homogeneous and inhomogeneous composite benchmark problems, where it is shown that the non-symmetric version of Nitsche's approach is the most robust in all settings.

keywords composite, microstructure, immersed, volumetric, Nitsche, non-symmetric Nitsche

1 Introduction

Composite analysis is an important class of problems in solid mechanics. For problems involving a great number of inclusions with irregular geometry, such as the CT-scan of a composite microstructure shown in Figure 1, it is time-consuming and difficult to construct a high quality body-fitting mesh for the traditional finite element method (FEM). On the other hand, non-body-fitting frameworks such as the immersed class of methods do not require a conforming discretization and therefore alleviate these difficulties.

The continuity condition at the inclusion interface in these methods can be imposed weakly by utilizing the Lagrange multiplier method [1–4], or Nitsche's method [5–11]. These approaches involve an interface contour integral

^c Department of Mechanical Engineering, The Pennsylvania State University, University Park, PA 16802, USA.

^{*}Corresponding author: email: mhillman@psu.edu

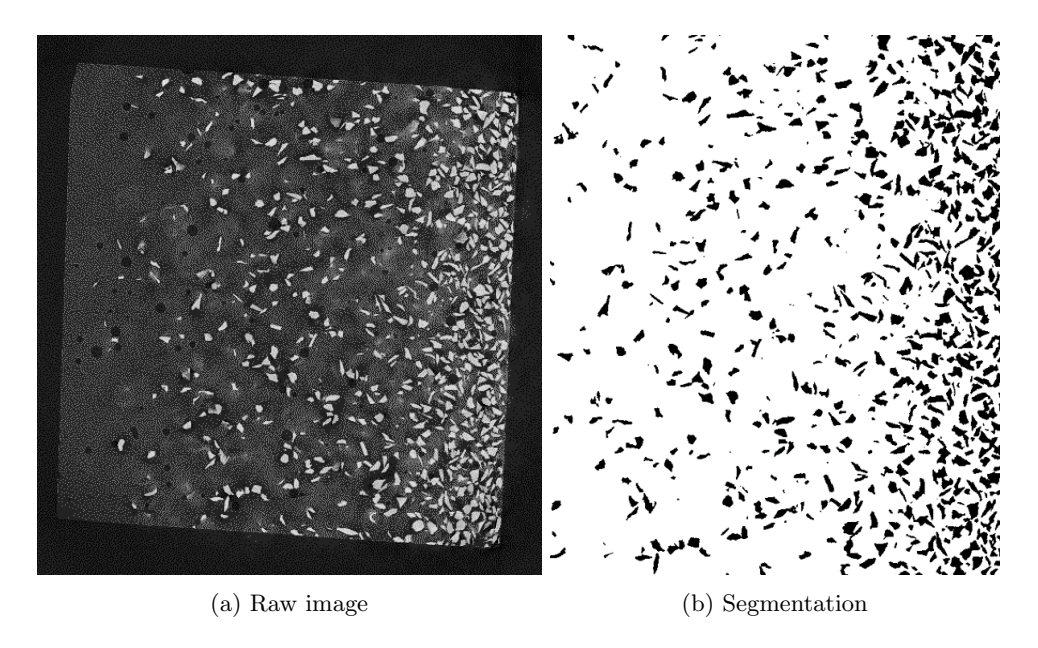


Figure 1: Micro-CT of a polymer-ceramic composite specimen.

and are herein termed surface-type. In [1,2], the Lagrange multiplier method was employed for the Dirichlet condition on the interface for the fictitious domain type approach. Hansbo et al. [3] introduced Lagrange multipliers for non-conforming finite element discretizations, and this was further developed as an interior penalty method for the purpose of stabilization [4]. Hansbo et al. [6,7] also developed a Nitsche method-based unfitted finite element method for the discontinuous problem. The method captures the interface by enforcing the jump condition. A robust Nistche formulation was proposed by Annavarapu et al. [8]. A weighting parameter was introduced to address the instability in the classical variational form of Nitsche's method for interface problems, and this approach was further extended to frictional sliding cases [9,10]. A Nitsche embedded-mesh method was introduced by Sanders et al. [11] for embedded finite element constraints, which alleviates mesh locking in the traditional mortar type approach. Li et al. [12] introduced the Cartesian grid method for the interface problem, which allows for both conforming and non-conforming meshes in FEM.

Enforcing the continuity condition or jump condition via traditional methods can still suffer from instabilities [13]. In [13], several traditional surface-type methods were studied, where the Lagrange multiplier method and penalty method were found to exhibit issues with both stability and accuracy. For stabilization in interface problems, Burman [14] developed a ghost penalty concept to enhance the robustness of the fictitious domain method, which is a commonly used technique for interface problems. A jump-stabilized Lagrange multiplier method with penalty-type stabilization was discussed by Burman et al. [4] for elliptic interface problems.

While many of these methods have shown to be effective, all of these methods fall into the class of surface-type, and for complicated composite topology such as the CT-scan shown in Figure 1, significant effort is still required to parameterize the interfaces between the inclusion and matrix domains.

Generalized FEM [15,16], or more generally, the class of partition of unity (PU) methods [17], are able to embed arbitrary enrichment functions extrinsically into a formulation such as FEM when solution features are known a priori, such as singularities, discontinuities, etc. This provides flexibility in constructing approximation functions relatively independent of a mesh, and can capture the interface conditions in inhomogeneous problems. Based on the concept of PU methods, the extended finite element method (XFEM) [18–20] considers local enrichment of the solution with the functions only embedded where special physical behavior exists. Arbitrary discontinuities can also be captured without remeshing, and the computational cost is not significantly increased due to the locally enriched shape functions [18,21]. Nevertheless, the class of PU methods with enrichments still requires special techniques to deal with issues such as quadrature, stability, blending, and time integration [22–25]. Meanwhile, these approaches still require parameterization of the interfaces at hand.

Although developed for fluids, among the methods which can avoid explicit definition of interfaces, the immersed boundary method (IBM) [26,27], which discretizes bodies independently without any conforming requirements, provides great potential for realizing the desired framework of effortless analysis of composites with arbitrarily complex microstructures. In the original immersed boundary method [26], the immersed body was assumed to be a volumeless fiber-like material that obtains its deformation by interpolating the velocity field of the fluid, exerting a force via an approximate Dirac delta function. The immersed concept was further developed into the immersed finite element method (IFEM) [28], where the immersed solid body is allowed to occupy a finite domain, and the interaction force

is given by the difference of the residual of the linear momentum equation in the immersed solid and background fluid, and the reproducing kernel was employed rather than the original approximate delta function to allow more complex interface geometries. IFEM has been further improved to consider the deformation in the immersed solid body instead of passively being displaced by the fluid velocity field [29]. In [30], the authors derived a new system of equations based on a weak form for IFEM, which avoids the adoption of an approximate Dirac delta function. Nevertheless, only theoretical work was provided in the paper without numerical examples.

Still under the general IBM framework, in [31] the continuity condition was approximately ensured by interpolating the velocity unknowns in the solid in terms of the background fluid using shape functions. As a result, however, the condition is only met at the solid's node positions unless a conforming mesh is used throughout the immersed domain. In [32] using meshfree methods for composite solids, the continuity condition across the interface was ensured at nodal positions by constructing convex generalized meshfree approximations that possess the Kronecker-delta property. Using this approach, the condition is also only met at nodal positions, and this method is also fairly complicated in implementation.

A volumetric-type constraint has been proposed by Blanco et. al. in [33] using Lagrange multipliers, and unlike IBM methods, this approach is mathematically well-justified by the fact that the weak form attests to the strong form of the problem. The surface continuity conditions are replaced by volumetric continuity in the overlapping domains. Due to the relative regularity of the approximations required in the weak formulation, the surface compatibility conditions are satisfied. However, extra degrees of freedom are introduced, and this method suffers from possible Ladyzhenskaya-Babuška-Brezzi (LBB) instabilities. Still within the volumetric continuity scope, the Arlequin method [34–37] considers the superposition of domains and the different domains are gluing together through the overlapping area. The total energy is conserved by the use of weighting parameter with the partition of unity feature. The volumetric continuity in the overlapped domain are enforced by using the Lagrange multiplier. In [38], Nguyen et. al. developed diffuse Nitsche method by converting the surface integral to the diffuse volumetric format under the standard Nitsche framework with the aid of phase field gradients. The normal vector appears in many interface integrals is approximated by the implicit phase field representation, which finally lead the weak form to be an approximate version.

In summary, the difficulties that remain an open problem in composite micro-structural analysis which the authors wish to address in this work are: (1) body-fitting meshes for conforming approaches; (2) parameterizing multiple and complex inclusion boundaries for surface-type and enriched approaches; (3) IBM methods which are not generally grounded in weak-form principles; and (4) The volumetric approach with associated LBB stability condition. Thus, a framework which can avoid the relative shortcomings of each of these classes of methods is highly desirable.

Based on the volumetric Lagrange multiplier approach in [33], in order to tackle the problem of simulating complicated composite inclusion problems, volumetric Nitsche methods are developed in this work as an effective solution to address the previously discussed difficulties. That is, within the general immersed framework, these methods work on non-body-fitting meshes and provide extreme flexibility in discretization necessary for relatively effortless model development of complex microstructures. The key idea of the proposed work is to first identify the weak form that attests to the strong form of the composite problem, with the continuity condition satisfied over the whole inclusion domain rather than at the interface. Then, the physical meaning of the Lagrange multiplier is identified following the Nitsche concept, which is then employed in the weak form to avoid extra degrees of freedom, and a penalty term is added for stability. The non-symmetric version of this method is also then developed. As will be seen, the proposed volumetric Nitsche/non-symmetric Nitsche methods require a background approximation space with C^1 continuity, which can be easily accomplished using meshfree [39], or isogeometric [40] approaches. Meanwhile, the method is also developed to allow C^0 continuity in the foreground to yield flexibility for the inclusion discretization. Because of the consistency of the weak forms developed, the resulting formulations are termed consistent immersed volumetric Nitsche (CIVN) methods in this work.

This paper is organized as follows. The strong form of the problem, and the weak form using the volumetric immersed approach are discussed in Section 2. The volumetric penalty approach and the proposed Nitsche/non-symmetric Nitsche approaches are then introduced in Section 3 and Section 4, respectively. In Section 5, discretized forms of these methods using the meshfree reproducing kernel approximation are presented. Numerical results are given in Section 6 to demonstrate the effectiveness of the proposed method, followed by conclusions and a discussion in Section 7.

2 Strong and weak form of composite inclusion problems

2.1 Strong form

Following the immersed framework, as shown Figure 2, the domains involved in the problem at hand are defined as follows: Ω_B is the background domain consisting of the total space occupied by both the matrix and inclusions, with boundary $\Gamma_B = \overline{\Gamma_g \cup \Gamma_t}$, and $\Gamma_g \cap \Gamma_t = \emptyset$, where Γ_g and Γ_t are the essential boundary, and natural boundary, respectively; $\Omega_F \subset \Omega_B$ is the immersed foreground domain; the physical matrix domain is defined by the compliment $\Omega_B \setminus \Omega_F$, and the interface between the two domains is denoted Γ_I . In this work, the subscript of field variables are used to denote where the variable is defined: "B" denotes background, "F" denotes foreground and "I" denotes the interface.

Here the background domain is a conceptually constructed domain for computational purposes, containing the entire physical space of the problem, with the material properties of the matrix.

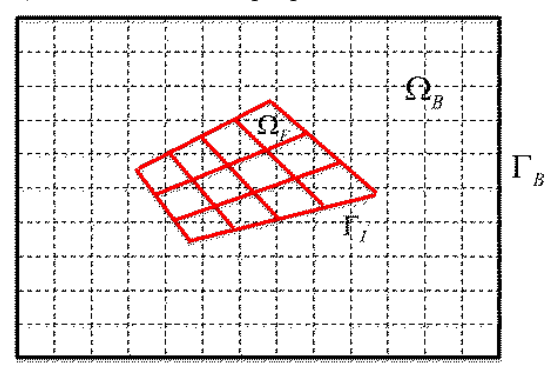


Figure 2: Two-dimensional illustration of the computational composite domain.

Without loss of generality, we have considered a single inclusion completely surrounded by a matrix, as illustrated in Figure 2. That is, Ω_F is completely immersed in the computational domain Ω_B yielding $\Gamma_B \cap \Gamma_I = \emptyset$. In addition, linear elastostatic problems are considered, which can later be extended to nonlinear or dynamic problems if desired. The corresponding strong form at hand is:

$$\nabla \cdot \boldsymbol{\sigma}_B + \boldsymbol{b}_B = \mathbf{0} \quad \text{in } \Omega_B \backslash \Omega_F \tag{1a}$$

$$\boldsymbol{u}_B = \bar{\boldsymbol{u}} \quad \text{on } \Gamma_{\boldsymbol{q}}$$
 (1b)

$$\boldsymbol{n} \cdot \boldsymbol{\sigma}_B = \bar{\boldsymbol{t}} \quad \text{on } \Gamma_{\boldsymbol{t}}$$
 (1c)

$$\nabla \cdot \boldsymbol{\sigma}_F + \boldsymbol{b}_F = \mathbf{0} \quad \text{in } \Omega_F \tag{1d}$$

$$n_I \cdot (\sigma_F - \sigma_B) = 0$$
 on Γ_I (1e)

$$u_B = u_F$$
 on Γ_I (1f)

where $\sigma_B = C_B : \varepsilon_B$ and $\sigma_F = C_F : \varepsilon_F$ are the Cauchy stress tensors in the background domain Ω_B and foreground domain Ω_F , respectively; $\varepsilon_B = \nabla^s u_B$ and $\varepsilon_F = \nabla^s u_F$ are the associated strain tensors and C_B and C_F are the associated elasticity tensors; b_B and b_F are the body force vectors in Ω_B and Ω_F respectively, u_B and u_F are the displacement vectors for the background and foreground domains respectively, \bar{u} is the prescribed displacement on the essential boundary Γ_g , \bar{t} is the given traction on the natural boundary Γ_t , and n_I denotes the outward normal vector of the inclusion domain Ω_F .

Eqs. (1a) and (1d) state the equilibrium equations of two domains, while the corresponding boundary conditions are specified in Eqs. (1b) and (1c). The compatibility conditions of traction and displacement are described in Eqs. (1e) and (1f), respectively.

2.2 Weak form

Following the key idea in [33] to apply the Lagrange multiplier in the immersed domain to enforce volumetric displacement compatibility rather than surface compatibility on the contour Γ_I , the variational formulation of a linear elastostatic composite inclusion problem defined by equations (1a) – (1f) is augmented, which leads to the following weak formulation: Find $\mathbf{u}_B \in H_q^1(\Omega_B)$, $\mathbf{u}_F \in H_q^1(\Omega_F)$, and $\lambda \in H^{-1}(\Omega_F)$, such that for all $\mathbf{w}_B \in H_0^1(\Omega_B)$,

 $\boldsymbol{w}_F \in H^1(\Omega_F)$ and $\boldsymbol{\gamma} \in H^{-1}(\Omega_F)$, the following equation holds [33]:

$$\int_{\Omega_{B}} \nabla^{s} \boldsymbol{w}_{B} : \boldsymbol{\sigma}_{B} d\Omega - \int_{\Omega_{B}} \boldsymbol{w}_{B} \cdot \boldsymbol{b}_{B} d\Omega + \int_{\Omega_{F}} \nabla^{s} \boldsymbol{w}_{F} : (\boldsymbol{\sigma}_{F} - \boldsymbol{\sigma}_{B}) d\Omega - \int_{\Omega_{F}} \boldsymbol{w}_{F} \cdot (\boldsymbol{b}_{F} - \boldsymbol{b}_{B}) d\Omega
- \int_{\Gamma_{t}} \boldsymbol{w}_{B} \cdot \bar{\boldsymbol{t}} d\Gamma + \int_{\Omega_{F}} \boldsymbol{\gamma} \cdot (\boldsymbol{u}_{F} - \boldsymbol{u}_{B}) d\Omega + \int_{\Omega_{F}} (\boldsymbol{w}_{F} - \boldsymbol{w}_{B}) \cdot \boldsymbol{\lambda} d\Omega = 0$$
(2)

where λ is the Lagrange multiplier with test function γ defined in the inclusion domain Ω_F , which enforces the continuity condition. Comparing the first and third terms, and the second and fourth terms, it can be seen that this form follows the immersed strategy, where the quadrature can be carried out on independent domains with independent quadrature rules without computing any intersections.

After performing integration by parts on the energy terms in Eq. (2), one obtains:

$$-\int_{\Omega_{B}\backslash\Omega_{F}} \boldsymbol{w}_{B} \cdot (\nabla \cdot \boldsymbol{\sigma}_{B} + \boldsymbol{b}_{B}) d\Omega + \int_{\Gamma_{t}} \boldsymbol{w}_{B} \cdot (\boldsymbol{n} \cdot \boldsymbol{\sigma}_{B} - \bar{\boldsymbol{t}}) d\Gamma - \int_{\Omega_{F}} \boldsymbol{w}_{B} \cdot (\nabla \cdot \boldsymbol{\sigma}_{B} + \boldsymbol{b}_{B} + \boldsymbol{\lambda}) d\Omega$$

$$-\int_{\Omega_{F}} \boldsymbol{w}_{F} \cdot [(\nabla \cdot \boldsymbol{\sigma}_{F} + \boldsymbol{b}_{F}) - (\nabla \cdot \boldsymbol{\sigma}_{B} + \boldsymbol{b}_{B}) - \boldsymbol{\lambda}] d\Omega + \int_{\Gamma_{I}} \boldsymbol{w}_{F} \cdot [\boldsymbol{n}_{I} \cdot (\boldsymbol{\sigma}_{F} - \boldsymbol{\sigma}_{B})] d\Gamma$$

$$+\int_{\Omega_{F}} \boldsymbol{\gamma} \cdot (\boldsymbol{w}_{F} - \boldsymbol{w}_{B}) d\Omega = 0.$$
(3)

Thus, from the above, the following strong form is recovered:

$$\mathbf{w}_B$$
 is arbitrary in $\Omega_B \backslash \Omega_F \Rightarrow \nabla \cdot \mathbf{\sigma}_B + \mathbf{b}_B = \mathbf{0}$ in $\Omega_B \backslash \Omega_F$ (4a)

$$\mathbf{w}_B$$
 is arbitrary on $\Gamma_t \Rightarrow \mathbf{n} \cdot \mathbf{\sigma}_B = \bar{\mathbf{t}}$ on Γ_t (4b)

$$\mathbf{w}_B$$
 is arbitrary in $\Omega_F \Rightarrow \nabla \cdot \mathbf{\sigma}_B + \mathbf{b}_B + \lambda = \mathbf{0}$ in Ω_F (4c)

$$\mathbf{w}_F$$
 is arbitrary in $\Omega_F \Rightarrow (\nabla \cdot \mathbf{\sigma}_F + \mathbf{b}_F) - (\nabla \cdot \mathbf{\sigma}_B + \mathbf{b}_B) - \lambda = \mathbf{0}$ in Ω_F (4d)

$$\mathbf{w}_F$$
 is arbitrary on $\Gamma_I \Rightarrow \mathbf{n}_I \cdot (\mathbf{\sigma}_B - \mathbf{\sigma}_F) = \mathbf{0}$ on Γ_I (4e)

$$\gamma$$
 is arbitrary in $\Omega_F \Rightarrow u_F = u_B$ in Ω_F . (4f)

It is obvious that equations (4a), (4b), and (4e) are nothing but equation (1a), (1c), and (1e). Here equation (4f) implies that $\mathbf{u}_B = \mathbf{u}_F$ on the interface (i.e. Eq. (1f) is satisfied). Finally, subtracting equation (4c) from (4d) indicates (1d) is met, which completes the proof of equivalence of Eqs. (4a)-(4f) and (1a)-(1f), provided that $\mathbf{u}_B \in H_g^1(\Omega_B)$. Note that this particular weak form directly embeds the traction compatibility condition without additional effort or explicit description of the interface.

Remark 1 It appears that the form of Eq. (2) cannot be derived from a variational viewpoint. That is, there is apparently no potential associated with Eq. (2). In [33], the constrained variational equation with Lagrange multiplier was augmented with additional terms after-the-fact, which enables Eq. (2) to recover (1a)-(1f). In other words without this augmentation of the variational equation, which does not appear to be obvious, the strong form is not recovered.

Although no contour integral terms are introduced, the two main concerns about the Lagrange multiplier approach, introducing extra degrees of freedom, and potentially suffering from LBB instability, remain to be addressed, which motivates the derivation of the formulations in the following sections.

3 Immersed volumetric penalty method

To eliminate the additional degrees of freedom caused by the Lagrange multiplier, one strategy could be to directly replace the Lagrange multiplier terms by a penalty constraint leading to the following form:

$$\int_{\Omega_{B}} \nabla^{s} \boldsymbol{w}_{B} : \boldsymbol{\sigma}_{B} d\Omega - \int_{\Omega_{B}} \boldsymbol{w}_{B} \cdot \boldsymbol{b}_{B} d\Omega + \int_{\Omega_{F}} \nabla^{s} \boldsymbol{w}_{F} : (\boldsymbol{\sigma}_{F} - \boldsymbol{\sigma}_{B}) d\Omega - \int_{\Omega_{F}} \boldsymbol{w}_{F} \cdot (\boldsymbol{b}_{F} - \boldsymbol{b}_{B}) d\Omega - \int_{\Gamma_{t}} \boldsymbol{w}_{B} \cdot \bar{\boldsymbol{t}} d\Gamma + \beta \int_{\Omega_{F}} (\boldsymbol{w}_{B} - \boldsymbol{w}_{F}) \cdot (\boldsymbol{u}_{B} - \boldsymbol{u}_{F}) d\Omega = 0.$$
(5)

That is, the last term in Eq. (5) is equivalent to taking the variational derivative of the penalty-type residual

$$R_{\beta} = \beta/2 \int_{\Omega_F} (\boldsymbol{u}_B - \boldsymbol{u}_F) \cdot (\boldsymbol{u}_B - \boldsymbol{u}_F) d\Omega.$$
 (6)

To examine if the weak form with a volumetric penalty constraint is equivalent to the strong form, one can perform integration by parts on Eq. (5) and obtain:

$$-\int_{\Omega_{B}\backslash\Omega_{F}} \boldsymbol{w}_{B} \cdot (\nabla \cdot \boldsymbol{\sigma}_{B} + \boldsymbol{b}_{B}) d\Omega + \int_{\Gamma_{t}} \boldsymbol{w}_{B} \cdot (\boldsymbol{n} \cdot \boldsymbol{\sigma}_{B} - \bar{\boldsymbol{t}}) d\Gamma + \int_{\Gamma_{I}} \boldsymbol{w}_{F} \cdot [\boldsymbol{n}_{I} \cdot (\boldsymbol{\sigma}_{F} - \boldsymbol{\sigma}_{B})] d\Gamma - \int_{\Omega_{F}} \boldsymbol{w}_{B} \cdot [(\nabla \cdot \boldsymbol{\sigma}_{B} + \boldsymbol{b}_{B}) + \beta(\boldsymbol{u}_{F} - \boldsymbol{u}_{B})] d\Omega + \int_{\Omega_{F}} \boldsymbol{w}_{F} \cdot [\nabla \cdot (\boldsymbol{\sigma}_{B} - \boldsymbol{\sigma}_{F}) + (\boldsymbol{b}_{B} - \boldsymbol{b}_{F}) + \beta(\boldsymbol{u}_{F} - \boldsymbol{u}_{B})] d\Omega = 0.$$
(7)

Based on Eq. (7), the following strong form is found:

$$\mathbf{w}_B$$
 is arbitrary in $\Omega_B \backslash \Omega_F \Rightarrow \nabla \cdot \mathbf{\sigma}_B + \mathbf{b}_B = \mathbf{0}$ in $\Omega_B \backslash \Omega_F$ (8a)

$$\mathbf{w}_B$$
 is arbitrary on $\Gamma_t \Rightarrow \mathbf{n} \cdot \mathbf{\sigma}_B = \bar{\mathbf{t}}$ on Γ_t (8b)

$$\mathbf{w}_B$$
 is arbitrary in $\Omega_F \Rightarrow \nabla \cdot \mathbf{\sigma}_B + \mathbf{b}_B + \beta(\mathbf{u}_F - \mathbf{u}_B) = \mathbf{0}$ in Ω_F (8c)

$$\mathbf{w}_F$$
 is arbitrary in $\Omega_F \Rightarrow -(\nabla \cdot \mathbf{\sigma}_F + \mathbf{b}_F) + (\nabla \cdot \mathbf{\sigma}_B + \mathbf{b}_B) + \beta(\mathbf{u}_F - \mathbf{u}_B) = \mathbf{0}$ in Ω_F (8d)

$$\mathbf{w}_F$$
 is arbitrary on $\Gamma_I \Rightarrow \mathbf{n}_I \cdot (\mathbf{\sigma}_B - \mathbf{\sigma}_F) = \mathbf{0}$ on Γ_I . (8e)

The combination of Eqs. (8c) and (8d) immediately gives:

$$\nabla \cdot \boldsymbol{\sigma}_F + \boldsymbol{b}_F = \mathbf{0} \quad \text{in } \Omega_F. \tag{9}$$

Eqs. (8a)-(8b) and (8e)-(9) take the same form as the strong form found by Lagrange multiplier. However, for the compatibility condition of displacement described in Eq. (4f), Eq. (8c) implies:

$$\boldsymbol{u}_F = \boldsymbol{u}_B - \frac{1}{\beta} (\nabla \cdot \boldsymbol{\sigma}_B + \boldsymbol{b}_B) \tag{10}$$

which means, as $\beta \to \infty$, $u_F \to u_B$. When β is small, the compatibility condition of displacement cannot be recovered, which leads to the derivation of the immersed volumetric Nitsche methods in the next section.

4 Consistent immersed volumetric Nitsche methods

This section develops a volumetric Nitsche method to eliminate the aforementioned underlying issues with the Lagrange multiplier and penalty approaches. The strategy to achieve this is first to determine the physical quantity that the volumetric Lagrange multiplier represents and use this quantity to replace it in the original weak form such that no additional degrees of freedom are introduced. A penalty term is then added to ensure coercivity, which is similar to the surface-type Nitsche method for enforcing essential boundary conditions [41]. Since these methods are derived from the Lagrange multiplier approach which has shown to be consistent with the strong form, the proposed Nitsche method will inherit the consistency.

4.1 Immersed volumetric Nitsche method

Following the derivation in section 2.2, the following physical quantities associated with the Lagrange multiplier are apparently:

$$\lambda = -(\nabla \cdot \boldsymbol{\sigma}_B + \boldsymbol{b}_B) \quad \text{in } \Omega_F$$
 (11a)

$$\lambda = (\nabla \cdot \boldsymbol{\sigma}_F + \boldsymbol{b}_F) - (\nabla \cdot \boldsymbol{\sigma}_B + \boldsymbol{b}_B) \quad \text{in } \Omega_F.$$
(11b)

As discussed previously, a solution to these two equations can be found by subtracting one from another:

$$\nabla \cdot \boldsymbol{\sigma}_F + \boldsymbol{b}_F = \mathbf{0} \quad \text{in } \Omega_F \tag{12}$$

which is the equilibrium of the inclusion in the inclusion domain. Using this result, it seems that both Eq. (11a) and Eq. (11b) indicate that the physical meaning of Lagrange multiplier is the (negative) residual of the background domain in the foreground.

However, we posit that a convex linear combination of the two meanings can be taken, similar to the Nitsche methods employed for surfaces in [11], and later verify the consistency between weak and strong form:

$$\lambda = (1 - \alpha) \left[(\nabla \cdot \boldsymbol{\sigma}_F + \boldsymbol{b}_F) - (\nabla \cdot \boldsymbol{\sigma}_B + \boldsymbol{b}_B) \right] - \alpha (\nabla \cdot \boldsymbol{\sigma}_B + \boldsymbol{b}_B)$$

$$\equiv (1 - \alpha) \left[\boldsymbol{r}(\boldsymbol{u}_F) - \boldsymbol{r}(\boldsymbol{u}_b) \right] - \alpha \boldsymbol{r}(\boldsymbol{u}_B)$$

$$= (1 - \alpha) \boldsymbol{r}(\boldsymbol{u}_F) - \boldsymbol{r}(\boldsymbol{u}_B)$$
(13)

where $r(u) \equiv \nabla \cdot \boldsymbol{\sigma} + \boldsymbol{b}$ denotes the residual of the equilibrium equations. Using this notation, one may write Eq. (3) as:

$$-\int_{\Omega_{B}\backslash\Omega_{F}} \boldsymbol{w}_{B} \cdot (\nabla \cdot \boldsymbol{\sigma}_{B} + \boldsymbol{b}_{B}) d\Omega + \int_{\Gamma_{t}} \boldsymbol{w}_{B} \cdot (\boldsymbol{n} \cdot \boldsymbol{\sigma}_{B} - \bar{\boldsymbol{t}}) d\Gamma - \int_{\Omega_{F}} \boldsymbol{w}_{B} \cdot (\boldsymbol{r}(\boldsymbol{u}_{B}) + \boldsymbol{\lambda}) d\Omega$$

$$-\int_{\Omega_{F}} \boldsymbol{w}_{F} \cdot [\boldsymbol{r}(\boldsymbol{u}_{F}) - \boldsymbol{r}(\boldsymbol{u}_{B}) - \boldsymbol{\lambda}] d\Omega + \int_{\Gamma_{I}} \boldsymbol{w}_{F} \cdot [\boldsymbol{n}_{I} \cdot (\boldsymbol{\sigma}_{F} - \boldsymbol{\sigma}_{B})] d\Gamma$$

$$+\int_{\Omega_{F}} \boldsymbol{\gamma} \cdot (\boldsymbol{w}_{F} - \boldsymbol{w}_{B}) d\Omega = 0.$$
(14)

Then with Eq. (13) in hand, we have for Eq. (14):

$$-\int_{\Omega_{B}\backslash\Omega_{F}} \boldsymbol{w}_{B} \cdot (\nabla \cdot \boldsymbol{\sigma}_{B} + \boldsymbol{b}_{B}) d\Omega + \int_{\Gamma_{t}} \boldsymbol{w}_{B} \cdot (\boldsymbol{n} \cdot \boldsymbol{\sigma}_{B} - \bar{\boldsymbol{t}}) d\Gamma - (1 - \alpha) \int_{\Omega_{F}} \boldsymbol{w}_{B} \cdot \boldsymbol{r}(\boldsymbol{u}_{F}) d\Omega$$

$$-\alpha \int_{\Omega_{F}} \boldsymbol{w}_{F} \cdot \boldsymbol{r}(\boldsymbol{u}_{F}) d\Omega + \int_{\Gamma_{I}} \boldsymbol{w}_{F} \cdot [\boldsymbol{n}_{I} \cdot (\boldsymbol{\sigma}_{F} - \boldsymbol{\sigma}_{B})] d\Gamma + \int_{\Omega_{F}} [(1 - \alpha)\boldsymbol{r}(\boldsymbol{w}_{F}) - \boldsymbol{r}(\boldsymbol{w}_{B})] \cdot (\boldsymbol{u}_{F} - \boldsymbol{u}_{B}) d\Omega = 0.$$
(15)

So, in place of Eqs. (4c) and (4d):

$$\mathbf{w}_B$$
 is arbitrary in $\Omega_F \Rightarrow (1 - \alpha)\mathbf{r}(\mathbf{u}_F) = \mathbf{0}$ in $\Omega_B \backslash \Omega_F$ (16a)

$$\mathbf{w}_F$$
 is arbitrary in $\Omega_F \Rightarrow \alpha \mathbf{r}(\mathbf{u}_F) = \mathbf{0}$ in $\Omega_B \backslash \Omega_F$. (16b)

Adding the above, we have $r(u_F) = 0$ which shows that the convex combination of (11a) and Eq. (11b) attests to the strong form. Thus the choice of α is arbitrary, at least in the continuous sense. In this work, we consider the choice of $\alpha = 1$ (that is Eq. (11a)), as it keeps the formulation as simple as possible, and so that the resulting formulation admits C^0 approximations (such as finite elements) for the foreground (in contrast to the choice of Eq. (11b), which would require higher-order continuity for both the foreground and background).

The essential idea of Nitsche's method is to use this physical meaning of the Lagrange multiplier to eliminate the extra variable, while adding a penalty term associated with the constraint, to ensure coercivity. With Eq. (2) and (13) in hand, and a penalty term in the form of $\beta \int_{\Omega_F} (\boldsymbol{w}_B - \boldsymbol{w}_F) \cdot (\boldsymbol{u}_B - \boldsymbol{u}_F) d\Omega$ added, and a volumetric Nitsche immersed formulation is obtained as: Find $\boldsymbol{u}_B \in H_g^2(\Omega_B)$ and $\boldsymbol{u}_F \in H^1(\Omega_F)$, such that for all $\boldsymbol{w}_B \in H_0^2(\Omega_B)$ and $\boldsymbol{w}_F \in H^1(\Omega_F)$, the following equation holds:

$$\int_{\Omega_{B}} \nabla^{s} \boldsymbol{w}_{B} : \boldsymbol{\sigma}_{B} d\Omega - \int_{\Omega_{B}} \boldsymbol{w}_{B} \cdot \boldsymbol{b}_{B} d\Omega + \int_{\Omega_{F}} \nabla^{s} \boldsymbol{w}_{F} : (\boldsymbol{\sigma}_{F} - \boldsymbol{\sigma}_{B}) d\Omega - \int_{\Omega_{F}} \boldsymbol{w}_{F} \cdot (\boldsymbol{b}_{F} - \boldsymbol{b}_{B}) d\Omega
- \int_{\Gamma_{t}} \boldsymbol{w}_{B} \cdot \bar{\boldsymbol{t}} d\Gamma - \int_{\Omega_{F}} \nabla \cdot \boldsymbol{\sigma}(\boldsymbol{w}_{B}) \cdot (\boldsymbol{u}_{F} - \boldsymbol{u}_{B}) d\Omega - \int_{\Omega_{F}} (\boldsymbol{w}_{F} - \boldsymbol{w}_{B}) \cdot (\nabla \cdot \boldsymbol{\sigma}_{B} + \boldsymbol{b}_{B}) d\Omega
+ \beta \int_{\Omega_{F}} (\boldsymbol{w}_{B} - \boldsymbol{w}_{F}) \cdot (\boldsymbol{u}_{B} - \boldsymbol{u}_{F}) d\Omega = 0.$$
(17)

Note that the background approximation in this weak form involves a residual-type term, and requires higher-order regularity than usually employed. A few possibilities are quadratic C^1 B-splines [40], or meshfree approximations [39].

Remark 2 Since the formulation does not emanate from a potential as mentioned previously, the derivation of Eq. (17) from a weighted residual viewpoint is provided in the Appendix, in order to provide generality and ground the method in weak-form principles. Then later, the proposed method can be developed for problems such as fluid-structure interaction using the weighted residual formulation.

Now, to prove consistency with the strong form of the proposed formulation, an integration by parts of Eq. (17) yields:

$$-\int_{\Omega_{B}\backslash\Omega_{F}} \boldsymbol{w}_{B} \cdot (\nabla \cdot \boldsymbol{\sigma}_{B} + \boldsymbol{b}_{B}) d\Omega + \int_{\Gamma_{t}} \boldsymbol{w}_{B} \cdot (\boldsymbol{n} \cdot \boldsymbol{\sigma}_{B} - \bar{\boldsymbol{t}}) d\Gamma + \int_{\Gamma_{I}} \boldsymbol{w}_{F} \cdot [\boldsymbol{n}_{I} \cdot (\boldsymbol{\sigma}_{F} - \boldsymbol{\sigma}_{B})] d\Gamma$$

$$-\int_{\Omega_{F}} \boldsymbol{w}_{F} \cdot [(\nabla \cdot \boldsymbol{\sigma}_{F} + \boldsymbol{b}_{F}) + \beta(\boldsymbol{u}_{B} - \boldsymbol{u}_{F})] d\Omega - \int_{\Omega_{F}} \nabla \boldsymbol{\sigma}(\boldsymbol{w}_{B}) \cdot (\boldsymbol{u}_{F} - \boldsymbol{u}_{B}) d\Omega$$

$$+\beta \int_{\Omega_{F}} \boldsymbol{w}_{B} \cdot (\boldsymbol{u}_{B} - \boldsymbol{u}_{F}) d\Omega = 0.$$
(18)

The associated strong form based on Eq. (18) is then:

$$\mathbf{w}_B$$
 is arbitrary in $\Omega_B \backslash \Omega_F \Rightarrow \nabla \cdot \mathbf{\sigma}_B + \mathbf{b}_B = \mathbf{0}$ in $\Omega_B \backslash \Omega_F$ (19a)

$$\mathbf{w}_B$$
 is arbitrary on $\Gamma_t \Rightarrow \mathbf{n} \cdot \mathbf{\sigma}_B = \overline{\mathbf{t}}$ on Γ_t (19b)

$$\mathbf{w}_B$$
 is arbitrary in $\Omega_F \Rightarrow \nabla \cdot \mathbf{\sigma}_F + \mathbf{b}_F + \beta(\mathbf{u}_B - \mathbf{u}_F) = \mathbf{0}$ in Ω_F (19c)

$$\mathbf{w}_F$$
 is arbitrary on $\Gamma_I \Rightarrow \mathbf{n}_I \cdot (\mathbf{\sigma}_B - \mathbf{\sigma}_F) = \mathbf{0}$ on Γ_I (19d)

$$\mathbf{w}_B$$
 is arbitrary in $\Omega_F \Rightarrow \mathbf{u}_F - \mathbf{u}_B = \mathbf{0}$ in Ω_F (19e)

$$\sigma(\mathbf{w}_B)$$
 is arbitrary in $\Omega_F \Rightarrow \mathbf{u}_F - \mathbf{u}_B = \mathbf{0}$ in Ω_F . (19f)

It is easy to observe that the combination of Eqs. (19c) and (19e) yields:

$$\nabla \cdot \boldsymbol{\sigma}_F + \boldsymbol{b}_F = \mathbf{0} \quad \text{in } \Omega_F. \tag{20}$$

Therefore the proposed weak form is fully consistent with the strong form of the composite problem (1). As such, the proposed formulation (17) is termed a consistent immersed volumetric Nitsche formulation.

4.2 Immersed volumetric non-symmetric Nitsche method

Alternatively, the formulation of a so-called non-symmetric Nitsche method can be obtained by changing the sign of the volumetric constraint term in Eq. (17), which yields:

$$\int_{\Omega_{B}} \nabla^{s} \boldsymbol{w}_{B} : \boldsymbol{\sigma}_{B} d\Omega - \int_{\Omega_{B}} \boldsymbol{w}_{B} \cdot \boldsymbol{b}_{B} d\Omega + \int_{\Omega_{F}} \nabla^{s} \boldsymbol{w}_{F} : (\boldsymbol{\sigma}_{F} - \boldsymbol{\sigma}_{B}) d\Omega - \int_{\Omega_{F}} \boldsymbol{w}_{F} \cdot (\boldsymbol{b}_{F} - \boldsymbol{b}_{B}) d\Omega
- \int_{\Gamma_{t}} \boldsymbol{w}_{B} \cdot \bar{\boldsymbol{t}} d\Gamma + \int_{\Omega_{F}} \nabla \cdot \boldsymbol{\sigma}(\boldsymbol{w}_{B}) \cdot (\boldsymbol{u}_{F} - \boldsymbol{u}_{B}) d\Omega - \int_{\Omega_{F}} (\boldsymbol{w}_{F} - \boldsymbol{w}_{B}) \cdot (\nabla \cdot \boldsymbol{\sigma}_{B} + \boldsymbol{b}_{B}) d\Omega
+ \beta \int_{\Omega_{F}} (\boldsymbol{w}_{B} - \boldsymbol{w}_{F}) \cdot (\boldsymbol{u}_{B} - \boldsymbol{u}_{F}) d\Omega = 0.$$
(21)

It can be shown that the weak form defined in Eq. (21) is still equivalent to the strong form following previous derivations. The non-symmetric Nitsche formulation can be derived from the weighted residual formulation as well, the details are provided in the Appendix.

Remark 3 Although the formulation is the so called non-symmetric version, the final assembled global matrix is non-symmetric for both volumetric approaches, which will be discussed in the next section.

5 Discretization

5.1 Reproducing kernel approximation

In this work, the meshfree reproducing kernel (RK) approximation [42] is used to discretize the Galerkin form of the newly derived weak forms, due to the regularity required in the present Nitsche formulations. The RK approximation $\boldsymbol{u}^h(\boldsymbol{x})$ of a vector function $\boldsymbol{u}(\boldsymbol{x})$ using a set of NP nodes in two dimensions is:

$$\boldsymbol{u}^{h}(\boldsymbol{x}) = \sum_{I \in \mathcal{S}_{\boldsymbol{x}}} \Psi_{I}(\boldsymbol{x}) \boldsymbol{d}_{I}$$
 (22)

where $\Psi_I(\mathbf{x})$ and \mathbf{d}_I are the shape function and the generalized displacement for the *I*th node, respectively, and $S_{\mathbf{x}} = \{I | \Psi_I(\mathbf{x}) \neq 0\}$. The shape function is constructed as a correction to the kernel function $\phi_a(\mathbf{x} - \mathbf{x}_I)$ with a compact support a:

$$\Psi_I(\mathbf{x}) = \mathbf{H}^{\mathsf{T}}(\mathbf{x} - \mathbf{x}_I)\mathbf{b}(\mathbf{x})\phi_a(\mathbf{x} - \mathbf{x}_I)$$
(23)

where $\mathbf{H}(\mathbf{x}) = \begin{bmatrix} 1, & x, & y, & x^2, & \cdots, & y^n \end{bmatrix}^\mathsf{T}$ is a column vector of complete nth order monomials, $\mathbf{b}(\mathbf{x})$ is a column vector containing all the associated unknown coefficients of each component in \mathbf{H} , and $\phi_a(\mathbf{x} - \mathbf{x}_I)$ is the kernel function which defines the locality and order of smoothness in the approximation. The cubic spline kernel function is employed in this work, which possesses C^2 continuity:

$$\phi_a(r) = \begin{cases} \frac{2}{3} - 4r^2 + 4r^3 & r \leqslant \frac{1}{2} \\ \frac{4}{3} - 4r + 4r^2 - \frac{4}{3}r^3 & \frac{1}{2} < r \leqslant 1 \\ 0 & r > 1 \end{cases}$$
 (24)

where $r \equiv \|\mathbf{x} - \mathbf{x}_I\|/a$ is a normalized relative distance. The unknown coefficient vector $\mathbf{b}(\mathbf{x})$ is determined by enforcing the *n*th order reproducing conditions:

$$\sum_{I \in \mathcal{S}_I} \Psi_I(\boldsymbol{x}) x_I^i y_I^j = x^i y^j, \quad i + j = 0, 1, \dots, n$$
(25)

which is equivalent to the following matrix form:

$$\sum_{I \in S_I} \Psi_I(\boldsymbol{x}) \boldsymbol{H}^{\mathsf{T}}(\boldsymbol{x} - \boldsymbol{x}_I) = \boldsymbol{H}^{\mathsf{T}}(\boldsymbol{0}). \tag{26}$$

Substituting Eq. (23) into Eq. (26) yields:

$$\boldsymbol{b}(\boldsymbol{x}) = \boldsymbol{M}^{-1}(\boldsymbol{x})\boldsymbol{H}(\boldsymbol{0}) \tag{27}$$

where $M(x) = \sum_{I \in S_x} H(x - x_I) H^{\mathsf{T}}(x - x_I) \phi_a(x - x_I)$ is the so-called moment matrix. Using Eq. (27), the RK shape function is obtained:

$$\Psi_I(\mathbf{x}) = \mathbf{H}^{\mathsf{T}}(\mathbf{0})\mathbf{M}^{-1}(\mathbf{x})\mathbf{H}(\mathbf{x} - \mathbf{x}_I)\phi_a(\mathbf{x} - \mathbf{x}_I). \tag{28}$$

Note that the order of smoothness of $\Psi_I(\boldsymbol{x})$ is inherited by the kernel function $\phi_a(\boldsymbol{x}-\boldsymbol{x}_I)$. Since the cubic spline kernel function employed is C^2 continuous, the shape function is also C^2 , which is sufficient for the proposed weak forms in Eqs. (17) and (21).

5.2 Matrix form

We choose to formulate the framework in two-dimensional space in this work, which can be extended to the threedimensional case without any special considerations. The trial and test function spaces of the weak forms in Eqs. (5), (17) and (21) are discretized by applying the RK approximation in the background domain Ω_B and the immersed foreground domain Ω_F :

$$\boldsymbol{u}_{B}^{h}(\boldsymbol{x}) = \begin{bmatrix} u_{Bx}^{h}(\boldsymbol{x}) \\ u_{By}^{h}(\boldsymbol{x}) \end{bmatrix} = \boldsymbol{N}_{B}\boldsymbol{d}_{B}$$
 (29a)

$$\boldsymbol{w}_{B}^{h}(\boldsymbol{x}) = \begin{bmatrix} w_{Bx}^{h}(\boldsymbol{x}) \\ w_{By}^{h}(\boldsymbol{x}) \end{bmatrix} = \boldsymbol{N}_{B}\boldsymbol{c}_{B}$$
 (29b)

$$\boldsymbol{u}_{F}^{h}(\boldsymbol{x}) = \begin{bmatrix} u_{Fx}^{h}(\boldsymbol{x}) \\ u_{By}^{h}(\boldsymbol{x}) \end{bmatrix} = \boldsymbol{N}_{F}\boldsymbol{d}_{F}$$
(29c)

$$\boldsymbol{w}_{F}^{h}(\boldsymbol{x}) = \begin{bmatrix} w_{Fx}^{h}(\boldsymbol{x}) \\ w_{Fy}^{h}(\boldsymbol{x}) \end{bmatrix} = \boldsymbol{N}_{F}\boldsymbol{c}_{F}$$
(29d)

with:

$$\mathbf{N} = \begin{bmatrix} \Psi_1 & 0 & \Psi_2 & 0 & \cdots & \Psi_{NP} & 0 \\ 0 & \Psi_1 & 0 & \Psi_2 & \cdots & 0 & \Psi_{NP} \end{bmatrix}$$
 (30a)

$$\boldsymbol{d} = \begin{bmatrix} d_{1x} & d_{1y} & d_{2x} & d_{2y} & \cdots & d_{NPx} & d_{NPy} \end{bmatrix}^{\mathsf{T}}$$
(30b)

$$\mathbf{c} = \begin{bmatrix} w_{1x} & w_{1y} & w_{2x} & w_{2y} & \cdots & w_{NPx} & w_{NPy} \end{bmatrix}^{\mathsf{T}}$$
 (30c)

where the subscripts are implied in the above.

Substituting the approximation for the test and trial functions (29) into the weak forms in Eqs. (5), (17) and (21), the following matrix forms are obtained:

$$(K + K^{\beta})d = F^{P} \text{ for penalty}$$
(31a)

$$(\mathbf{K} + \mathbf{K}^{\beta} + \mathbf{K}^{N} + (\mathbf{K}^{N})^{\mathsf{T}})\mathbf{d} = \mathbf{F}^{N} \text{ for Nitsche}$$
(31b)

$$(\mathbf{K} + \mathbf{K}^{\beta} + \mathbf{K}^{N} - (\mathbf{K}^{N})^{\mathsf{T}})\mathbf{d} = \mathbf{F}^{N}$$
 for non-symmetric Nitsche (31c)

where:

$$d = \begin{bmatrix} d_B \\ d_F \end{bmatrix}$$
 (32a)

$$\boldsymbol{K} = \begin{bmatrix} \boldsymbol{K}_{BB} & \mathbf{0} \\ \boldsymbol{K}_{FB} & \boldsymbol{K}_{FF} \end{bmatrix}$$
 (32b)

$$\boldsymbol{K}^{\beta} = \begin{bmatrix} \bar{\boldsymbol{K}}_{BB}^{\beta} & \bar{\boldsymbol{K}}_{BF}^{\beta} \\ \bar{\boldsymbol{K}}_{FB}^{\beta} & \bar{\boldsymbol{K}}_{FF}^{\beta} \end{bmatrix}$$
(32c)

$$\boldsymbol{K}^{N} = \begin{bmatrix} \bar{\boldsymbol{K}}_{BB} & \mathbf{0} \\ \bar{\boldsymbol{K}}_{FB} & \mathbf{0} \end{bmatrix}$$
 (32d)

$$\boldsymbol{F}^{P} = \begin{bmatrix} \boldsymbol{F}_{B}^{P} \\ \boldsymbol{F}_{F}^{P} \end{bmatrix} \tag{32e}$$

$$\boldsymbol{F}^{N} = \begin{bmatrix} \boldsymbol{F}_{B}^{N} \\ \boldsymbol{F}_{F}^{N} \end{bmatrix}$$
 (32f)

with the entries in the above given as:

$$\boldsymbol{K}_{BB} = \int_{\Omega_B} \boldsymbol{B}_B^{\mathsf{T}} \boldsymbol{C}_B \boldsymbol{B}_B \mathrm{d}\Omega \tag{33a}$$

$$\mathbf{K}_{FB} = -\int_{\Omega_F} \mathbf{B}_F^{\mathsf{T}} \mathbf{C}_B \mathbf{B}_B \mathrm{d}\Omega \tag{33b}$$

$$K_{FF} = \int_{\Omega_F} \mathbf{B}_F^{\mathsf{T}} \mathbf{C}_F \mathbf{B}_F d\Omega \tag{33c}$$

$$\bar{K}_{BB}^{\beta} = \beta \int_{\Omega_E} N_B^{\mathsf{T}} N_B d\Omega \tag{33d}$$

$$\bar{\boldsymbol{K}}_{BF}^{\beta} = -\beta \int_{\Omega_F} \boldsymbol{N}_B^{\mathsf{T}} \boldsymbol{N}_F d\Omega \tag{33e}$$

$$\bar{\boldsymbol{K}}_{FB}^{\beta} = -\beta \int_{\Omega_F} \boldsymbol{N}_F^{\mathsf{T}} \boldsymbol{N}_B d\Omega \tag{33f}$$

$$\bar{\boldsymbol{K}}_{FF}^{\beta} = \beta \int_{\Omega_F} \boldsymbol{N}_F^{\mathsf{T}} \boldsymbol{N}_F d\Omega \tag{33g}$$

$$\bar{K}_{BB} = \int_{\Omega_B} N_B^{\mathsf{T}} \bar{C}_B D_B d\Omega \tag{33h}$$

$$\bar{\mathbf{K}}_{FB} = -\int_{\Omega_F} \mathbf{N}_F^{\mathsf{T}} \bar{C}_B \mathbf{D}_B d\Omega \tag{33i}$$

$$\boldsymbol{F}_{B}^{P} = \int_{\Gamma_{t}} \boldsymbol{N}_{B}^{\mathsf{T}} \bar{\boldsymbol{t}} d\Gamma + \int_{\Omega_{B}} \boldsymbol{N}_{B}^{\mathsf{T}} \boldsymbol{b}_{B} d\Omega$$
 (33j)

$$\boldsymbol{F}_{F}^{P} = \int_{\Omega_{-}} \boldsymbol{N}_{F}^{\mathsf{T}} (\boldsymbol{b}_{F} - \boldsymbol{b}_{B}) d\Omega$$
 (33k)

$$\boldsymbol{F}_{B}^{N} = \int_{\Gamma_{\bullet}} \boldsymbol{N}_{B}^{T} \bar{\boldsymbol{t}} d\Gamma + \int_{\Omega_{B}} \boldsymbol{N}_{B}^{T} \boldsymbol{b}_{B} d\Omega - \int_{\Omega_{E}} \boldsymbol{N}_{B}^{T} \boldsymbol{b}_{B} d\Omega$$
(331)

$$\boldsymbol{F}_F^N = \int_{\Omega_F} \boldsymbol{N}_F^\mathsf{T} \boldsymbol{b}_F \mathrm{d}\Omega \tag{33m}$$

where the Ith components of \boldsymbol{B} and \boldsymbol{D} are:

$$\boldsymbol{B}_{I} = \begin{bmatrix} \Psi_{I,x} & 0 & \Psi_{I,y} \\ 0 & \Psi_{I,y} & \Psi_{I,x} \end{bmatrix}^{\mathsf{T}}$$
(34a)

$$\mathbf{D}_{I} = \begin{bmatrix} \Psi_{I,xx} & \Psi_{I,xy} & \Psi_{I,yy} & 0 & 0 & 0 \\ 0 & 0 & 0 & \Psi_{I,xx} & \Psi_{I,yy} & \Psi_{I,yy} \end{bmatrix}^{\mathsf{T}}.$$
 (34b)

Furthermore, the material matrices are given by the following:

$$C = \frac{\tilde{E}}{1 - \tilde{\nu}^2} \begin{bmatrix} 1 & \tilde{\nu} & 0\\ \tilde{\nu} & 1 & 0\\ 0 & 0 & (1 - \tilde{\nu})/2 \end{bmatrix}$$
 (35a)

$$\bar{C} = \frac{\tilde{E}}{1 - \tilde{\nu}^2} \begin{bmatrix} 1 & 0 & (1 - \tilde{\nu})/2 & 0 & (1 + \tilde{\nu})/2 & 0 \\ 0 & (1 + \tilde{\nu})/2 & 0 & (1 - \tilde{\nu})/2 & 0 & 1 \end{bmatrix}$$
(35b)

where:

$$\tilde{E} = \begin{cases} E & \text{for plane stress} \\ E/(1-\nu^2) & \text{for plane strain} \end{cases}$$
 (36a)

$$\tilde{E} = \begin{cases}
E & \text{for plane stress} \\
E/(1-\nu^2) & \text{for plane strain}
\end{cases}$$

$$\tilde{\nu} = \begin{cases}
\nu & \text{for plane stress} \\
\nu/(1-\nu) & \text{for plane strain}
\end{cases}$$
(36a)

in which E and ν are Young's modulus and Poisson's ratio of the material respectively.

In the matrix form, the stiffness matrix K^N comes from the change of the Lagrange multiplier to its physical meaning. Meanwhile, K^{β} is a result of the penalty terms in both formulations. A special component in the stiffness matrix K common to all formulations is K_{FB} , which works as a natural coupling matrix that builds the connection between domains via the consistent weak enforcement of the traction compatibility. Thus the additional off-diagonal coupling terms enforce displacement capability; the terms absent from the penalty method in K^N are required for consistency of the strong form.

Remark 4 Both Nitsche formulations contain K^N , which is not symmetric. Therefore the change of sign in the "non-symmetric" version of Nitsche's method does change the symmetry of the formulation, and nothing is lost by this change of signs in terms of the symmetry of the global system.

Remark 5 To evaluate the matrix forms for the immersed method, numerical quadrature needs to be carried out for Eqs. (33a) - (33m). Since the weak forms proposed have been derived from (2), which has followed the immersed strategy, one can generate two sets of independent quadrature points for the domain integrals, and there is no need to compute the intersections of the integration cells.

Remark 6 The coercivity of immersed volumetric Nitsche and non-symmetric Nitsche methods are achieved by adding the penalty type term $\beta \int_{\Omega_F} (\boldsymbol{w}_B - \boldsymbol{w}_F) \cdot (\boldsymbol{u}_B - \boldsymbol{u}_F) d\Omega$. From the discretized matrix formulations in Eq. (31), the penalty type term will eventually be formed a positive definite matrix \boldsymbol{K}^{β} in Eq. (32c) to increase the positive definiteness of the solution.

Remark 7 The choice of β has the effect on both accuracy and stability of the numerical solution. As the component of matrices $N \sim 1$, $B \sim 1/h$ and $D \sim 1/h^2$, the integrands of matrices K and K^N are not at the same order with K^{β} , where h is the nodal spacing. Therefore, in this paper, the normalized $\beta^{\text{nor}} = \beta/h^2$, $\beta \in [E^B, E^F]$ is employed to replace the original fixed β to avoid the overlarge or small penalty matrix, which can cause the inaccurate and unstable simulation results, where E^B and E^F represent the Young's modulus in matrix and inclusion domains, respectively.

6 Numerical examples

In this section, several benchmark problems are tested to evaluate the effectiveness of the proposed methods of immersed Nitsche and immersed non-symmetric Nitsche, which are compared to the pure penalty method. The essential boundary conditions are enforced using the traditional Nitsche's method. All penalty parameters are normalized by the nodal spacing h as h^{-2} . Unless otherwise stated, linear basis in the RK approximation is employed, along with cubic spline kernels. The error in the L_2 norm, H^1 semi-norm (denoted H_{s1}), and energy norm used to evaluate the methods are defined as follows:

$$L_{2} \text{ error} = \left(\int_{\Omega_{B} \setminus \Omega_{F}} (\boldsymbol{u}_{B} - \boldsymbol{u}_{B}^{h}) \cdot (\boldsymbol{u}_{B} - \boldsymbol{u}_{B}^{h}) d\Omega + \int_{\Omega_{F}} (\boldsymbol{u}_{F} - \boldsymbol{u}_{F}^{h}) \cdot (\boldsymbol{u}_{F} - \boldsymbol{u}_{F}^{h}) d\Omega \right)^{1/2}$$

$$(37a)$$

$$U_{B} = \sum_{A} \left[\nabla_{A} (\boldsymbol{u}_{B} - \boldsymbol{u}_{B}^{h}) + [\nabla_{A} (\boldsymbol{u}_{B} - \boldsymbol{u}_{B}^{h})] d\Omega + \int_{\Omega_{F}} [\nabla_{A} (\boldsymbol{u}_{B} - \boldsymbol{u}_{F}^{h})] d\Omega \right]^{1/2}$$

$$H_{s1} \text{ error} = \left(\int_{\Omega_B \setminus \Omega_F} \left[\nabla \otimes (\boldsymbol{u}_B - \boldsymbol{u}_B^h) \right] : \left[\nabla \otimes (\boldsymbol{u}_B - \boldsymbol{u}_B^h) \right] d\Omega + \int_{\Omega_F} \left[\nabla \otimes (\boldsymbol{u}_F - \boldsymbol{u}_F^h) \right] : \left[\nabla \otimes (\boldsymbol{u}_F - \boldsymbol{u}_F^h) \right] d\Omega \right)^{1/2}$$

$$(37b)$$

Energy error =
$$\left(\int_{\Omega_B \setminus \Omega_F} (\boldsymbol{\varepsilon}_B - \boldsymbol{\varepsilon}_B^h) : (\boldsymbol{\sigma}_B - \boldsymbol{\sigma}_B^h) d\Omega + \int_{\Omega_F} (\boldsymbol{\varepsilon}_F - \boldsymbol{\varepsilon}_F^h) : (\boldsymbol{\sigma}_F - \boldsymbol{\sigma}_F^h) d\Omega\right)^{1/2}$$
(37c)

which are evaluated by 20-point Gaussian quadrature in 1D and 5×5 point Gaussian quadrature in 2D.

6.1 1D bi-material elastic bar problem

Analogous to the 1D example in [43], consider a 1D inhomogeneous bar with length L=1 with a hard inclusion in the middle, as shown in Figure 3. A distributed body force acts on the entire bar. The governing equation of this problem reads:

$$\begin{cases}
\frac{d}{dx}(\ddot{E}\frac{du}{dx}) + b(x) = 0 \quad]0, L[\\ u(0) = 0\\ u(L) = \bar{u}
\end{cases}$$
(38)

where \tilde{E} is Young's modulus taking the following form:

$$\bar{E} = \begin{cases} E^{(2)} & x \in [L/3, 2L/3] \\ E^{(1)} & \text{else} \end{cases} . \tag{39}$$

To study the effectiveness of proposed methods, the material constant in the matrix domain is selected as $E^{(1)} = 1$, while the inclusion material property $E^{(2)}$ is varied to yield different cases. The bar is subject to two essential boundary conditions u(0) = 0 and $u(L) = \bar{u}$. The analytical solution can be obtained by integrating the governing equation (3). With the aid of the left boundary condition, the analytical solution can be found as:

$$u(x) = \int_0^x \frac{1}{\tilde{E}} \left[c_0 - \int_0^t b(\tau) d\tau \right] dt \tag{40}$$

where c_0 is an integration constant that can be determined by the second boundary condition $u(L) = \bar{u}$. Since c_0 and \bar{u} are related, in this problem, we manufacture \bar{u} by setting $c_0 = 1$. Three meshfree discretizations are constructed as shown in Figure 4 for analysis. Here, non-conforming background and foreground domain discretizations are first considered. Linear basis and a normalized support size of 1.8 are taken in the meshfree approximation.

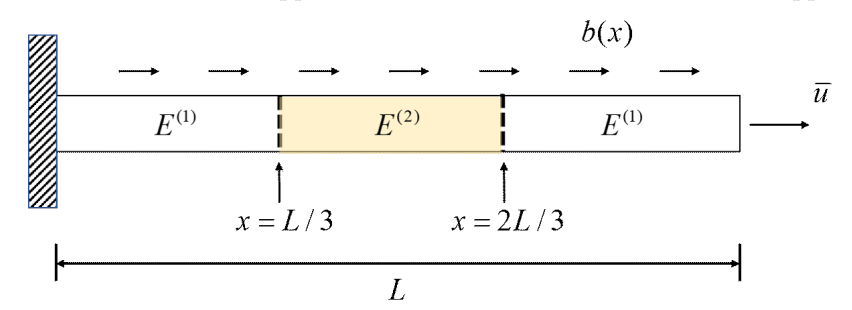


Figure 3: Description of inhomogeneous 1D bar problem.

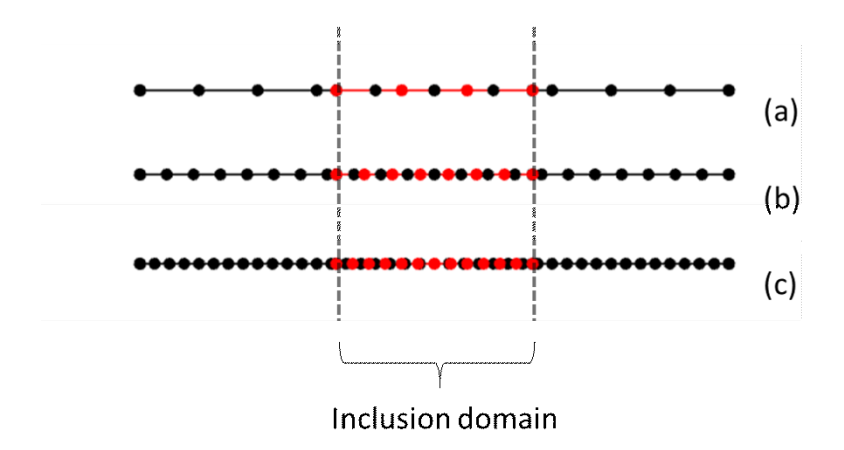


Figure 4: Non-conforming meshfree discretization for 1D bar problem: (a) 15 particles; (b) 31 particles; (c) 54 particles.

6.1.1 Piece-wise linear displacement in bar

First, a body force of zero is considered, i.e., b(x) = 0, which is can be considered a linear patch test for both homogeneous and inhomogeneous problems, depending on the ratio of moduli.

Taking the homogeneous case, i.e., $E^{(2)}/E^{(1)} = 1$, which is the standard (homogeneous) linear patch test, the results for the displacement and strain with varying β are shown in Figures 5 and 6, respectively, for the finest discretization in Figure 4(c). It can be seen that when the penalty parameter is zero, the penalty method yields spurious results in the displacement field. However, the strain field is close to exact. Recall that for all three methods, the traction compatibility is consistently weakly enforced, but the displacement compatibility is only consistently enforced for the Nitsche methods. For all other cases, all other methods yield acceptable results and the patch test is essentially passed. Importantly, this also serves as a verification that the Nitsche methods do in fact attest to the strong form of the composite problem.

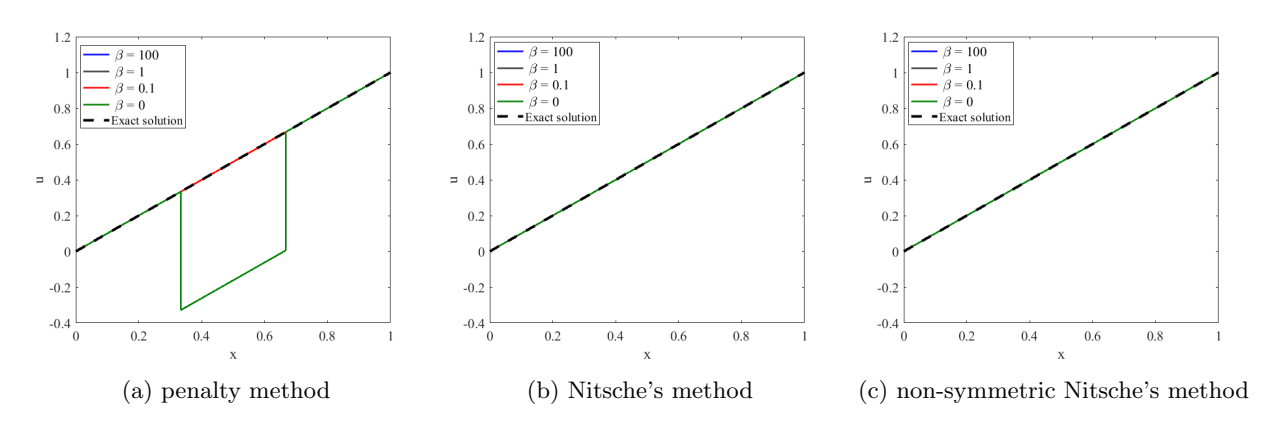


Figure 5: Displacement results for the 1D bi-material bar problem with zero body force, $E^{(2)}/E^{(1)} = 1$.

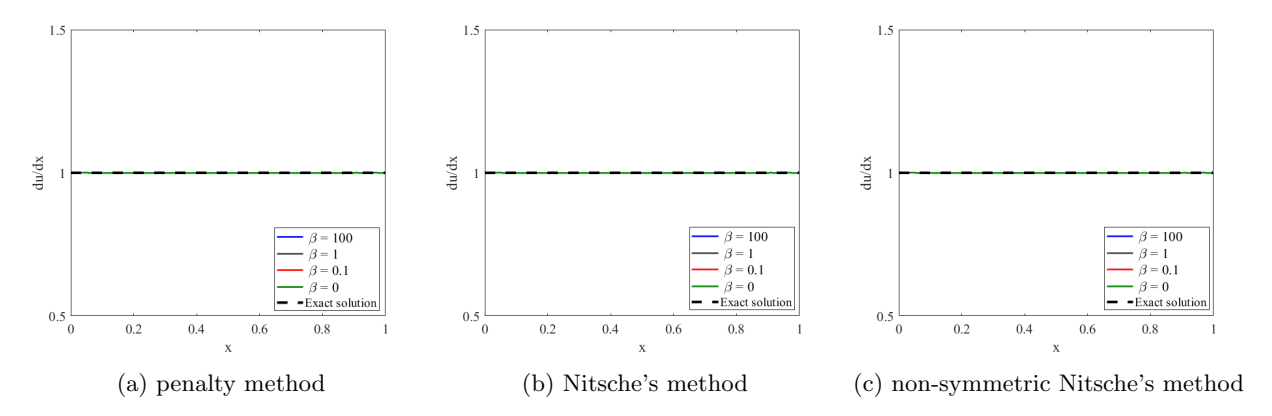


Figure 6: Strain results for the 1D bi-material bar problem with zero body force, $E^{(2)}/E^{(1)} = 1$.

Next, the inhomogeneous case is tested for the discretization in Figure 4(c) with $E^{(2)}/E^{(1)} = 100$, with comparisons of displacement and strain shown in Figures 7 and 8, respectively. Due to the inhomogeneity, the exact solution is piece-wise linear in the displacement field and is discontinuous in the strain field. The solution via the penalty method is strongly dependent on the penalty parameter. The proposed Nitsche methods agree well with the analytical solution in both displacement and strain, even when the penalty parameter is relatively small. In addition, the solutions are not strongly dependent on the choice of parameter overall.

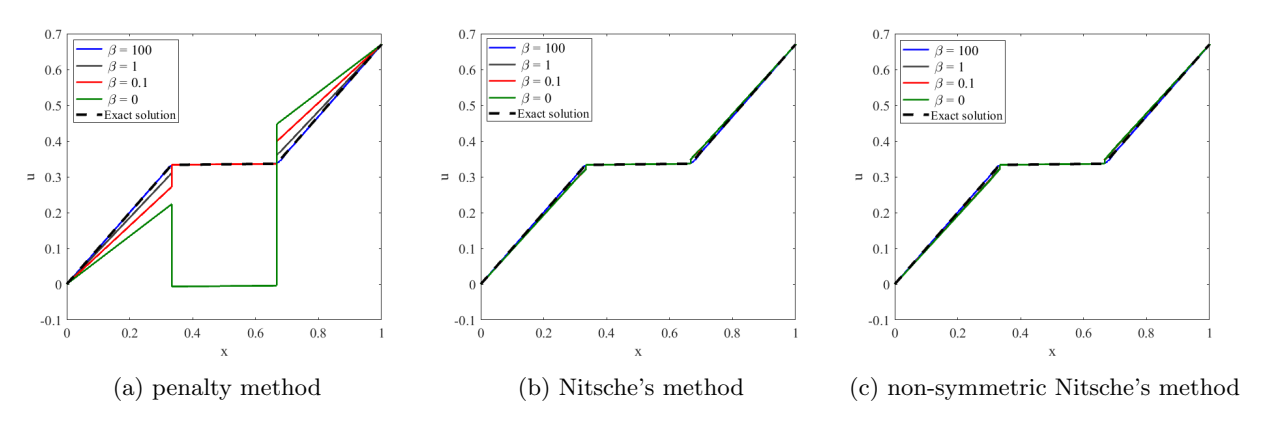


Figure 7: Displacement results for the 1D bi-material bar problem with zero body force, $E^{(2)}/E^{(1)} = 100$.

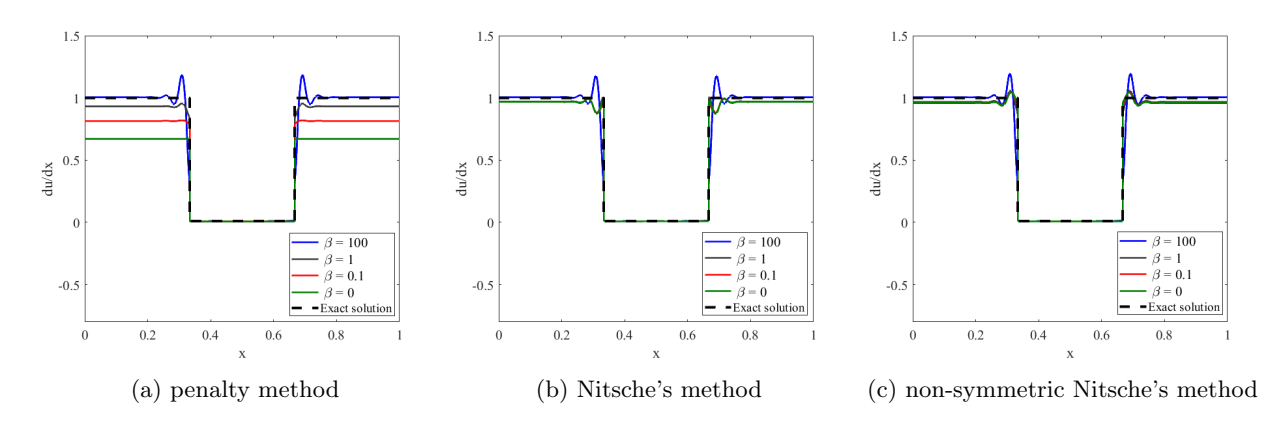


Figure 8: Strain results for the 1D bi-material bar problem with zero body force, $E^{(2)}/E^{(1)} = 100$.

6.1.2 High-order displacement in bar

To further study the effectiveness of the proposed method, a cubic body force of $b(x) = 1 + 25x - 10x^2 + x^3$, is considered to provide a convergence analysis, since now the highest order of polynomials in the true solution is 5, while linear basis is employed.

First, a homogeneous material is considered to assess the convergence of the proposed methods in problems sufficiently regular that yield the standard error estimate i.e., with optimal convergence rates associated with the

order of approximation employed. The corresponding convergence studies for different penalty parameters are given in Figures 9 and 10 for the displacement and strain respectively. From the results, the optimal second-order convergence rates in the L_2 norm and first-order rate in the H_{s1} can be obtained by the proposed Nitsche methods when the material is homogeneous. The error in the solution is relatively insensitive to the value of the parameter, and the optimal rate is obtained in all cases. In contrast, the penalty method is slightly more sensitive to the value of the parameter, and does not converge in the displacement for $\beta = 0$.

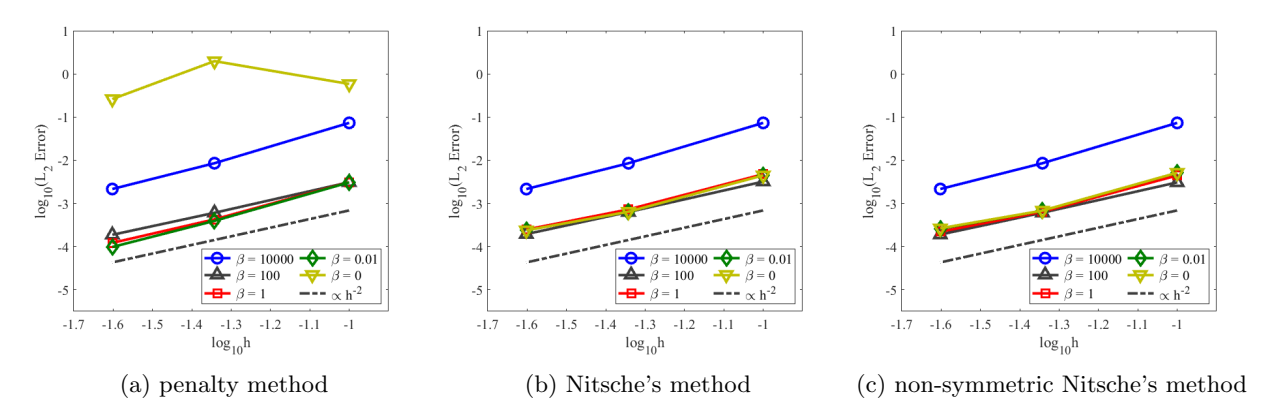


Figure 9: Convergence comparison of L_2 error norm for the 1D bi-material bar problem with different penalty parameters, $E^{(2)}/E^{(1)} = 1$.

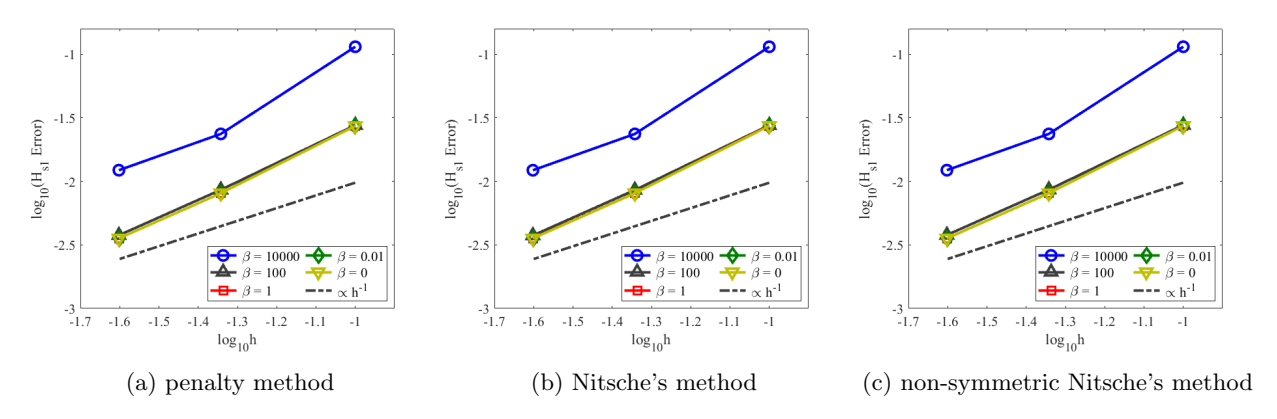


Figure 10: Convergence comparison of H_{S1} error norm for the 1D bi-material bar problem with different penalty parameters, $E^{(2)}/E^{(1)} = 1$.

Next, $E^{(2)}/E^{(1)}=100$ is chosen, and the rate of convergence drops by half as the regularity of the true solution is decreased, as shown in Figures 11 and 12. Both figures indicate that a lower penalty parameter will lead to the inaccurate solution for the penalty method, and in this case the solution is highly sensitive to the value of the parameter. However, both Nitsche and non-symmetric Nitsche's method enable a much more flexible choice of penalty parameter, with solutions either converging at either half optimal rate as expected, or in some cases exhibiting super convergence. Likely, an optimal value can be obtained using a related eigenvalue analysis [44], but this is considered beyond the scope of this work.

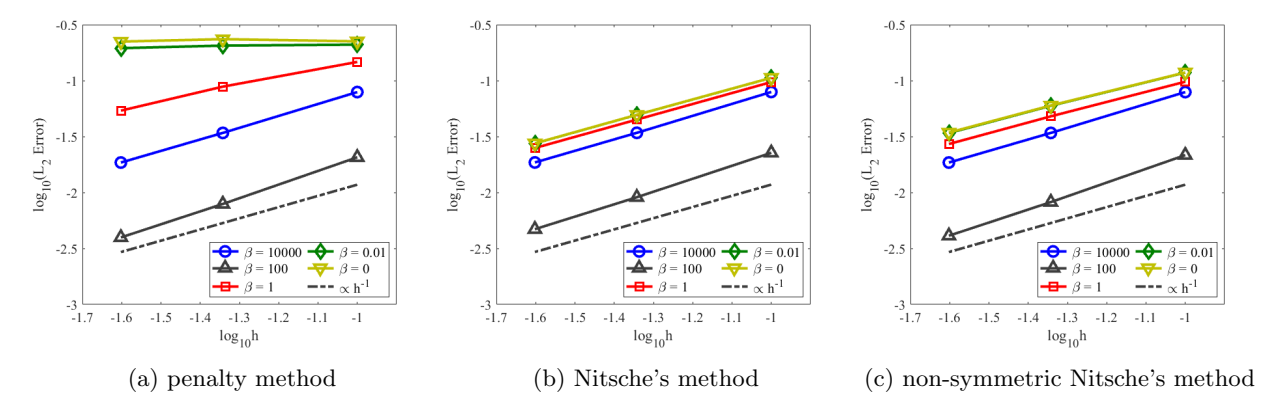


Figure 11: Convergence comparison of L_2 error norm for the 1D bi-material bar problem with different penalty parameters, $E^{(2)}/E^{(1)} = 100$.

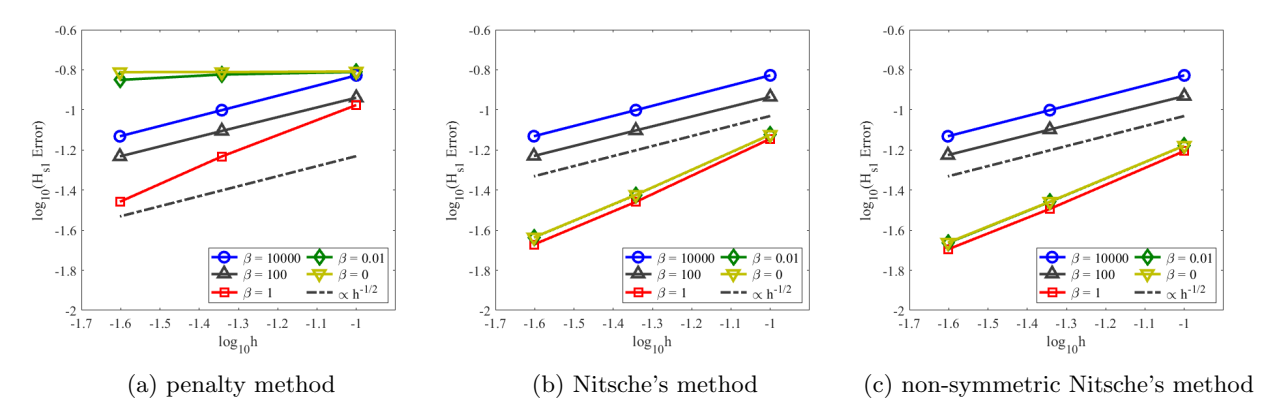


Figure 12: Convergence comparison of H_{S1} error norm for the 1D bi-material bar problem with different penalty parameters, $E^{(2)}/E^{(1)} = 100$.

A comparison of the distribution of displacement and strain are shown in Figures 13 and 14 respectively, for the finest discretization shown in Figure 4(c). It can be seen that the solution of the pure penalty method is sensitive to the penalty parameter, and that a sufficiently large value is necessary for good accuracy. Meanwhile, the Nitsche methods are not sensitive to the parameter, and yield solutions which are accurate across the range of values chosen.

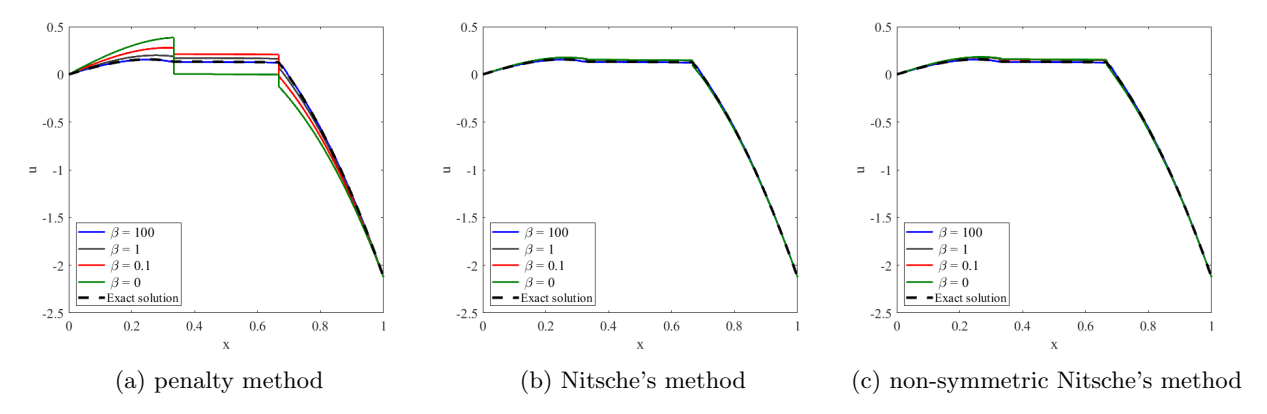


Figure 13: Displacement results comparison for the 1D bi-material bar problem with cubic body force and different penalty parameters, $E^{(2)}/E^{(1)} = 100$.

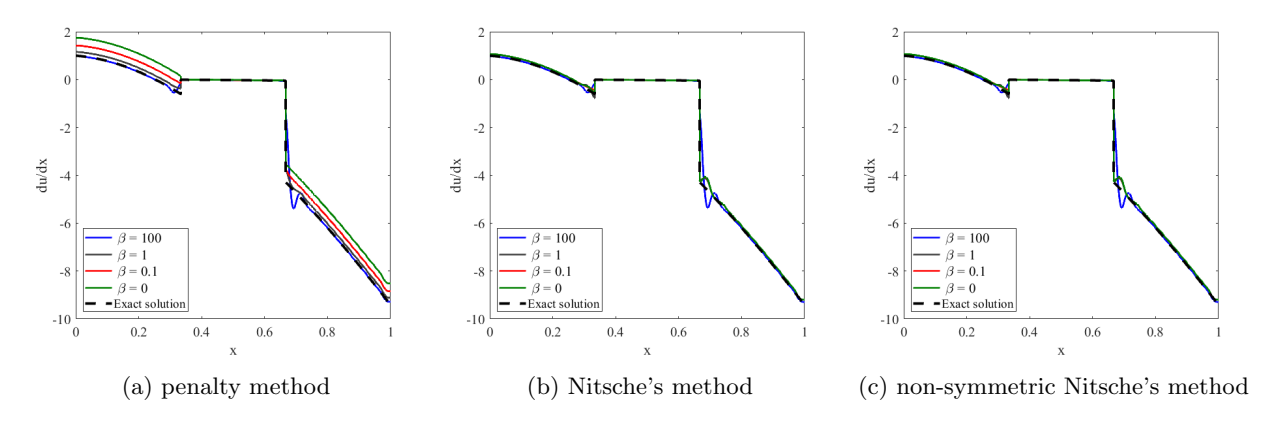


Figure 14: Strain results comparison for the 1D bi-material bar problem with cubic body force and different penalty parameters, $E^{(2)}/E^{(1)} = 100$.

6.1.3 High-order displacement in bar with only foreground refinement

In contrast to the previous convergence comparison, in this subsection, the consistency of proposed methods is further studied. The L_2 error comparisons are provided in Table 1 and Table 2 for homogeneous and inhomogeneous problems under the only foreground refinement as depicted in Figure 15, respectively. As can be noticed from the tables, since the discretization in background is fixed, the global L_2 error norm is influenced by the error from background, even the foreground discretization is sufficient fine. For the homogeneous case in Table 1, the error starts to decrease under the first refinement (from discretization 1 to discretization 2) but remains same after the second refinement (from discretization 2 to discretization 3). For the inhomogeneous case in Table 2, the result does not converge. Both L_2 error results indicate that the foreground and background solutions are coupled through the coupling terms.

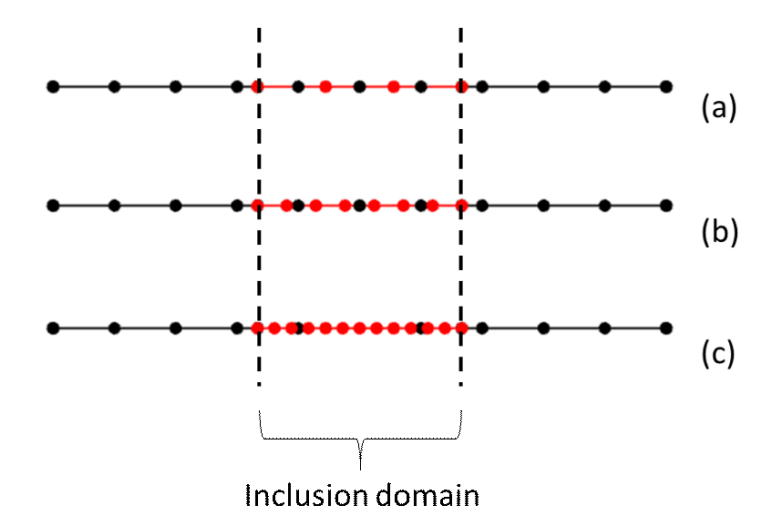


Figure 15: Non-conforming meshfree discretization for 1D bar problem with the only refinement on inclusion domain: (a) 15 particles; (b) 18 particles; (c) 24 particles.

Table 1: L_2 error norms for the 1D bi-material under the refinement from Figure 15 with $\beta = E^{(1)}$, $E^{(2)}/E^{(1)} = 1$.

	Discretization 1	Discretization 2	Discretization 3
Penalty method	3.102E-3	1.988E-3	1.978E-3
Nitsche's method	4.746E-3	2.055E-3	2.074E-3
Non-symmetric Nitsche's method	4.439E-3	2.110E-3	2.109E-3

Table 2: L_2 error norms for the 1D bi-material under the refinement from Figure 15 with $\beta = E^{(1)}$, $E^{(2)}/E^{(1)} = 100$.

	Discretization 1	Discretization 2	Discretization 3
Penalty method	1.469E-1	1.469E-1	1.469E-1
Nitsche's method	9.707E-2	9.702 E-2	9.702E-2
Non-symmetric Nitsche's method	9.776E-2	9.783E-2	9.784E-2

6.1.4 High-order displacement in bar with conforming domains

Since both Nitsche methods outperform the penalty method so far and yield similar results, a conforming discretization as shown in Figure 16 is next considered to compare the two methods' robustness. Here, the position of the boundary nodes of the immersed domain are coincident with nodal locations in the background domain. A cubic body force is again considered with the inhomogeneous case of $E^{(2)}/E^{(1)} = 100$. As seen in Figure 17 and 18, inaccurate results are observed for the standard volumetric Nitsche's method, with solutions sensitive to the value of the penalty parameter. In particular, when low penalty parameters are employed, the solution is extremely inaccurate. This issue can be solved by using the non-symmetric Nitsche's method, where the solution is consistently accurate across all values.

Figure 16: Conforming meshfree discretization with 49 background particles and 25 foreground particles.

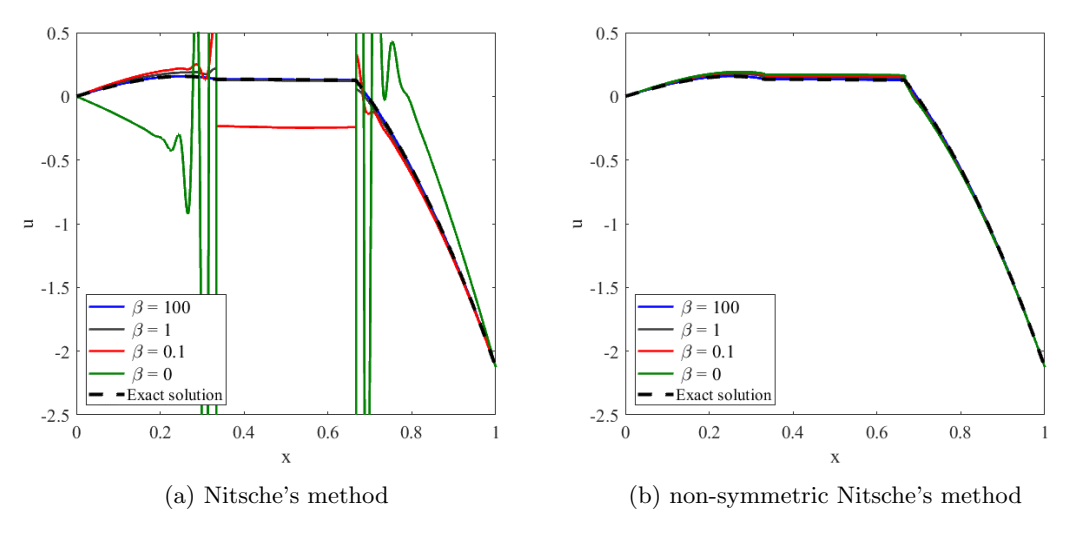
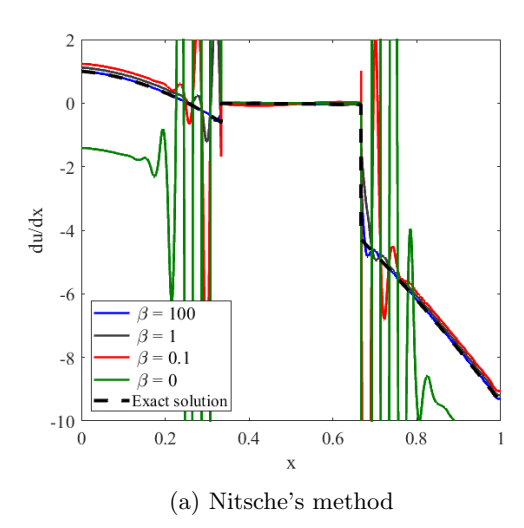
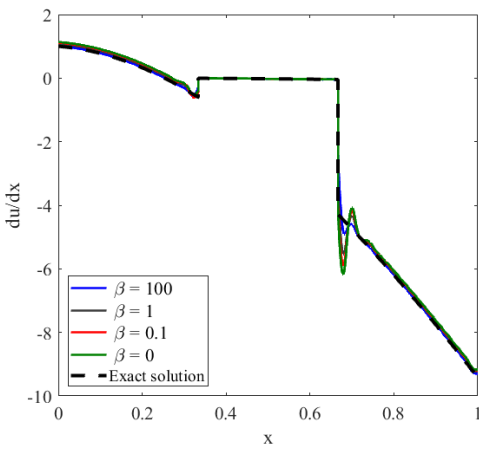


Figure 17: Displacement comparisons for the 1D bi-material bar problem with different penalty parameters and conforming meshfree discretization, $E^{(2)}/E^{(1)} = 100$.





(b) non-symmetric Nitsche's method

Figure 18: Gradient comparisons for the 1D bi-material bar problem with different penalty parameters and conforming meshfree discretization, $E^{(2)}/E^{(1)} = 100$.

To conclude, in these one dimensional examples, the penalty method performs relatively poorly and necessitates a large penalty parameter to yield reliable results. The non-symmetric Nitsche method is able to provide expected convergence rates and solutions that are not sensitive to the value of the penalty parameter, regardless of whether a conforming or non-conforming discretization is employed. This phenomenon is consistent with the one discussed by Burman in [45]. Since the choice of penalty parameter is not sensitive in non-symmetric Nitsche approach, this allows us for the choice without penalty term in the non-symmetric framework. The standard Nitche method performs equally well, but only as long as the discretization is non-conforming. Therefore the non-symmetric version should be the method of choice based on these examples.

6.2 Inhomogeneous heat conduction

Next, consider the inhomogeneous heat conduction problem shown in Figure 18, which is governed by the following strong form:

$$\begin{cases}
-\nabla \cdot (\kappa \nabla u) + m^2 r^{m-2} = 0 \text{ in } \Omega \\
\nabla u \cdot \boldsymbol{n} = \bar{t} \text{ on } \Gamma_{\boldsymbol{t}} \\
u = \bar{u} \text{ on } \Gamma_{\boldsymbol{g}}
\end{cases} \tag{41}$$

with r the distance to the origin and

$$\kappa = \begin{cases}
\kappa^{(2)} & r \in [0, r_0] \\
\kappa^{(1)} & \text{else}
\end{cases}$$
(42)

The exact solution corresponding to Eq. (41) is [12]:

$$u = \begin{cases} r^m/\kappa^{(2)} & r \leqslant r_0 \\ r^m/\kappa^{(1)} + (1/\kappa^{(2)} - 1/\kappa^{(1)})r_0^m & r > r_0 \end{cases}$$
 (43)

The boundary conditions in (41) are straightforwardly obtained from the above solution. Here, the free parameter m is set to three.

The three meshfree discretizations are plotted in Figure 19, which are utilized to perform a convergence study. Linear basis functions with a normalized support size of 1.3 are adopted. The mesh shown is not used for the construction of the approximation, but rather to clearly depict the relationship between the background and foreground domains.

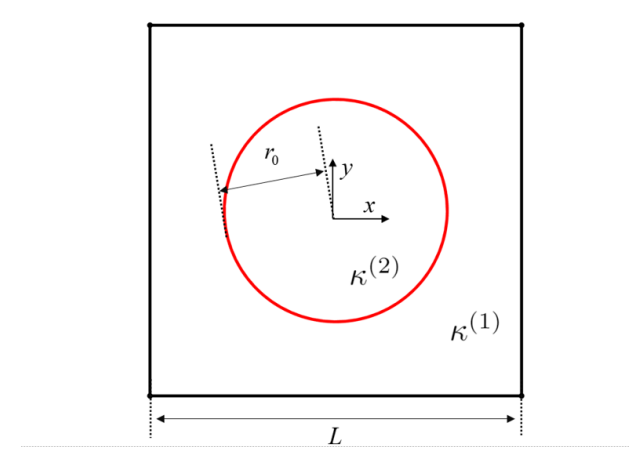


Figure 19: Problem description for the 2D inhomogeneous heat conduction problem.

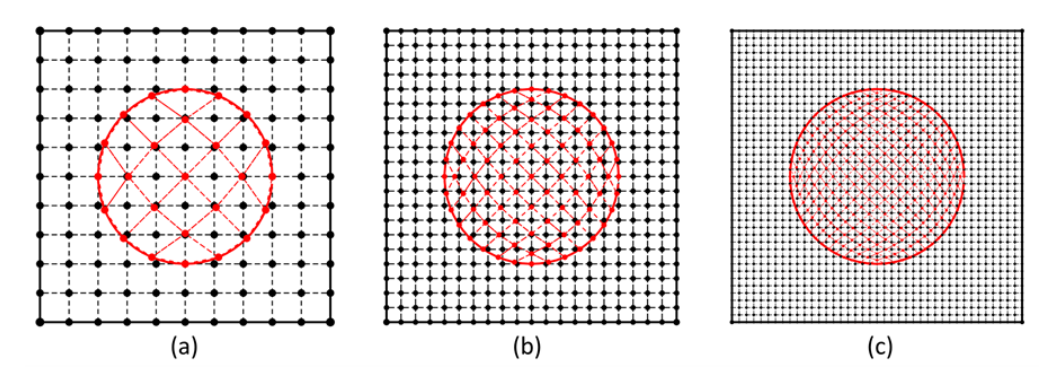


Figure 20: Meshfree discretizations for the 2D inhomogeneous heat conduction problem: (a)146 particles; (b) 522 particles; (c)1970 particles.

First, the convergence comparisons of volumetric penalty and Nitsche methods with different conductivity ratios are given in Figures 21 and 22, where the penalty parameter used in the simulation is selected as $\kappa^{(2)}$. From the figures, both L_2 and H_{s1} norms yield convergent results under the volumetric framework. For the case when ratio is 1, which means the problem is no longer inhomogeneous, the solution will posses sufficient regularity for optimal convergence rates. As the ratio increases, the rate is decreased to the expected rate of half the optimal. Among the methods tested, the penalty method and non-symmetric Nitsche's method preform the most consistently.

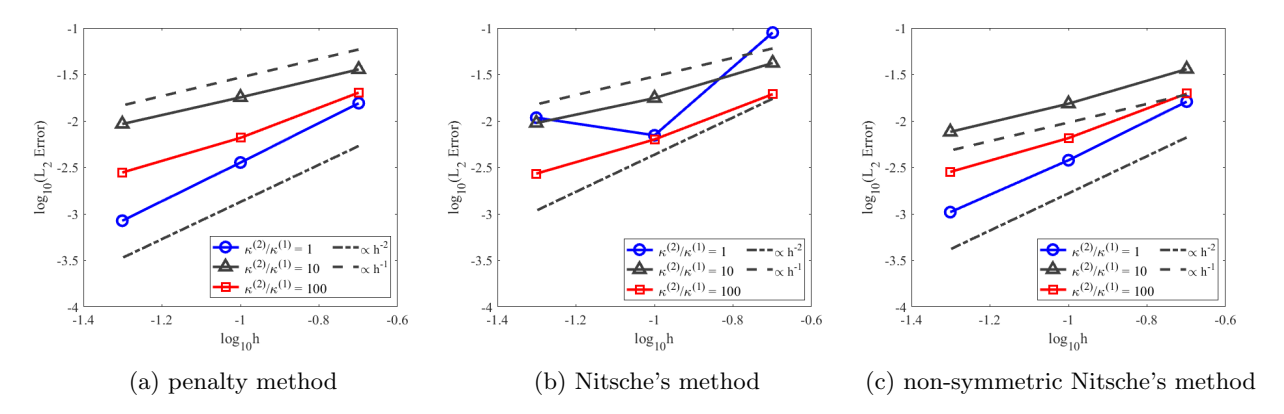


Figure 21: Convergence comparison of L_2 error norm for the 2D inhomogeneous heat problem with different ratios of conductivity, $\beta = \kappa^{(2)}$.

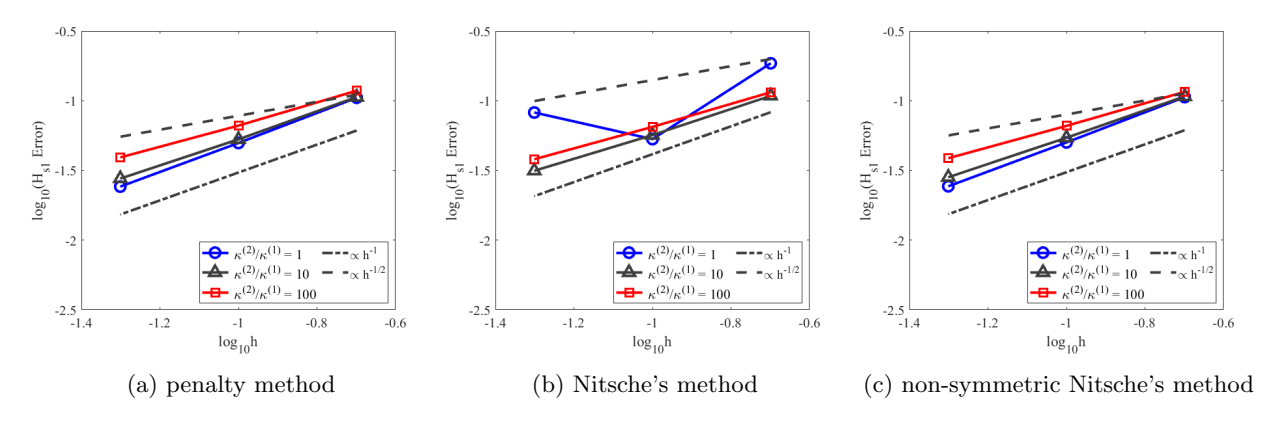


Figure 22: Convergence comparison of H_{S1} error norm for the 2D inhomogeneous heat problem with different ratio of conductivity, $\beta = \kappa^{(2)}$.

To further examine the performance of these methods, convergence comparisons varying the penalty parameters are shown in Figures 23 and 24. The results are consistent with the bar example: the error in the penalty method is seen to be highly sensitive to the penalty value. Meanwhile, the Nitsche methods are relatively insensative, with the non-symmetric version yielding the most consistent results. Here, superconvergence is again observed in the derivatives of the solution.

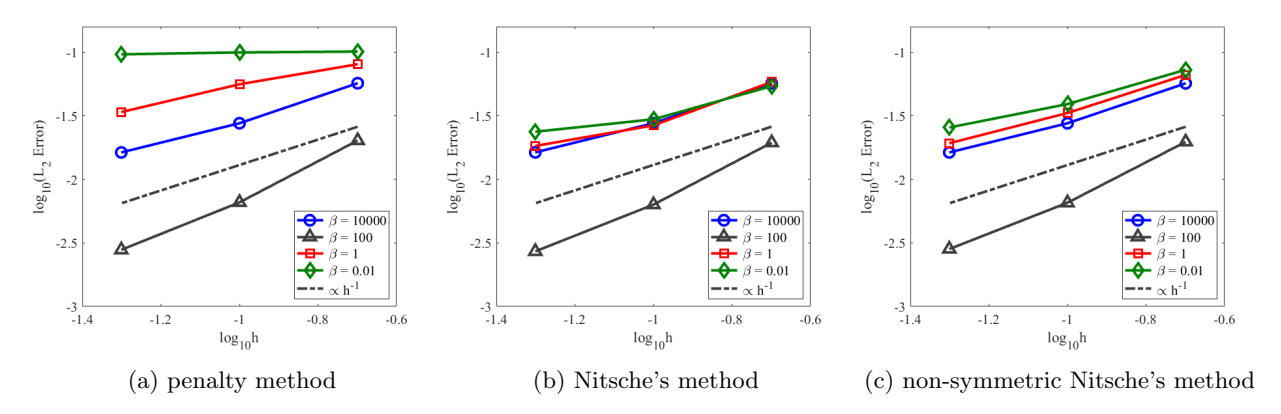


Figure 23: Convergence comparison of L_2 error norm for the 2D inhomogeneous heat problem with different penalty parameters, $\kappa^{(2)}/\kappa^{(1)} = 100$.

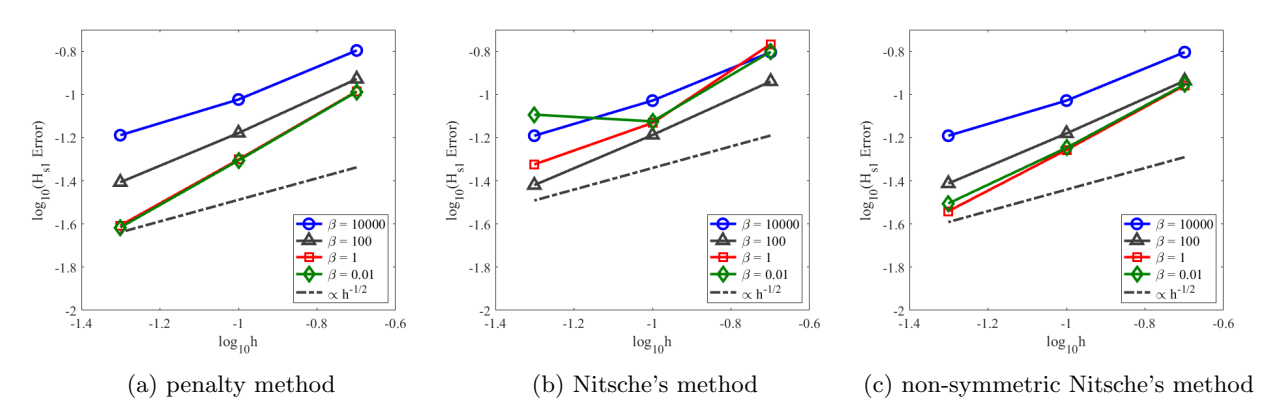


Figure 24: Convergence comparison of H_{s1} error norm for the 2D inhomogeneous heat problem with different penalty parameters, $\kappa^{(2)}/\kappa^{(1)} = 100$.

6.3 Inhomogeneous cell with multiple inclusions subject to tension loading

Consider the two-dimensional plane strain unit cell subject to tension loading shown in Figure 25. The cell is loaded on the top edge with a vertical displacement of 0.01m. The two immersed circular inclusion domains have the same material properties of Young's modulus $E^{(2)}=100.0$ MPa and Poisson's ratio $\nu^{(2)}=0.3$, while the matrix has different material properties of Young's modulus $E^{(1)}=0.1$ MPa and Poisson's ratio $\nu^{(1)}=0.3$. The material parameters, non-symmetric locations and varying sizes of the two inclusions are designed to create a complex solution field to further evaluate the proposed methods.

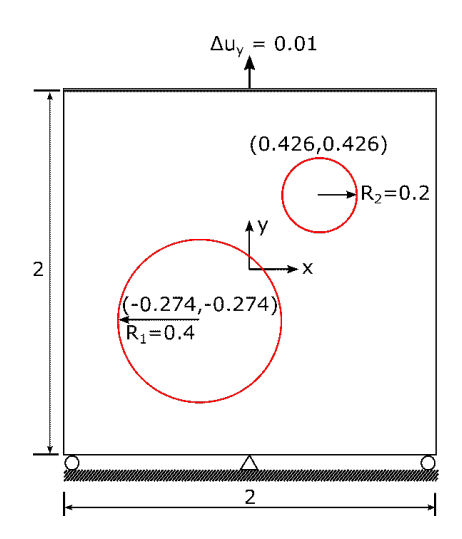


Figure 25: Schematic of unit cell with two inclusions subject to tension loading; units are m. Problem taken from [32].

Due to the complexity of the problem, there is no analytical solution available, so an FEM solution using a fine conforming mesh with 75,950 nodes and 75,449 elements (shown in Figure. 26) is utilized as a reference solution. L_2 convergence studies based on this solution are performed using the discretizations shown in Figure 27. Comparing Figures 26 and 27, it can be noticed that the conforming discretization yields highly non-uniform mesh near the interface, and as a result, the accuracy of simulation is decreased. Meanwhile, due to the process of conforming discretization, the efficiency modelling is decreased as well. On the contrary, the proposed algorithm allows non-conforming discretization (shown in Figure. 27), which can yield relatively uniform discretization in the background and foreground domain respectively.

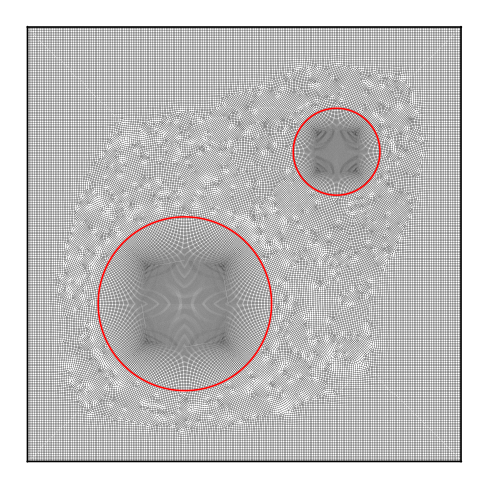


Figure 26: Conforming discretization of the unit cell with two inclusions: 75,950 nodes and 75,449 elements

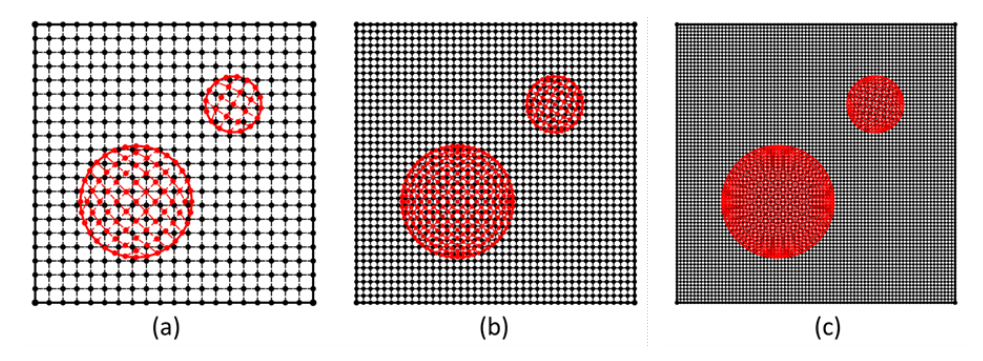


Figure 27: Non-conforming discretization of the unit cell with two inclusions: (a) 547 particles; (b) 2051 particles; (c) 7939 particles.

First, the average of the two Young's moduli is taken as the penalty parameter, and the results are shown in Table 3. Here, the error in the L_2 norm for all three approaches are comparable, consistent with previous results. It can be seen that the error is reduced by roughly half with each refinement, and the solution converges. This reduction in error corresponds to a rate of one as expected.

Table 3: L_2 error norms for the 2D inhomogeneous elasticity problem with $\beta = (E^{(1)} + E^{(2)})/2$.

	Discretization 1	Discretization 2	Discretization 3
Penalty method	2.107E-2	1.119E-2	5.109E-3
Nitsche's method	4.260E-2	4.315E-2	5.138E-3
Non-symmetric Nitsche's method	2.109E-2	1.120E-2	5.114E-3

Next, $\beta=E^{(1)}$ is selected, and the error norms are given in Table 4. Consistent with previous results, the non-symmetric volumetric Nitsche method yields the best performance. The error is decreased by roughly half, which indicates the expected convergence rate of one in the L_2 norm. In contrast, the penalty method and standard Nitsche method do not converge at this rate, and the Nitsche method is noticeably worse than the non-symmetric version.

The contours of the displacement magnitude of the reference and numerical solutions by using 547 meshfree particles are given in Figure 28, where the non-symmetric Nitsche's method yields the best displacement result among three methods.

Table 4: L_2 error norms for the 2D inhomogeneous elasticity problem with $\beta = E^{(1)}$.

	Discretization 1	Discretization 2	Discretization 3
Penalty method	5.659E-2	3.190E-2	1.686E-2
Nitsche's method	4.260E-2	4.315E-2	8.717E-3
Non-symmetric Nitsche's method	2.848E-2	1.445E-2	8.089E-3

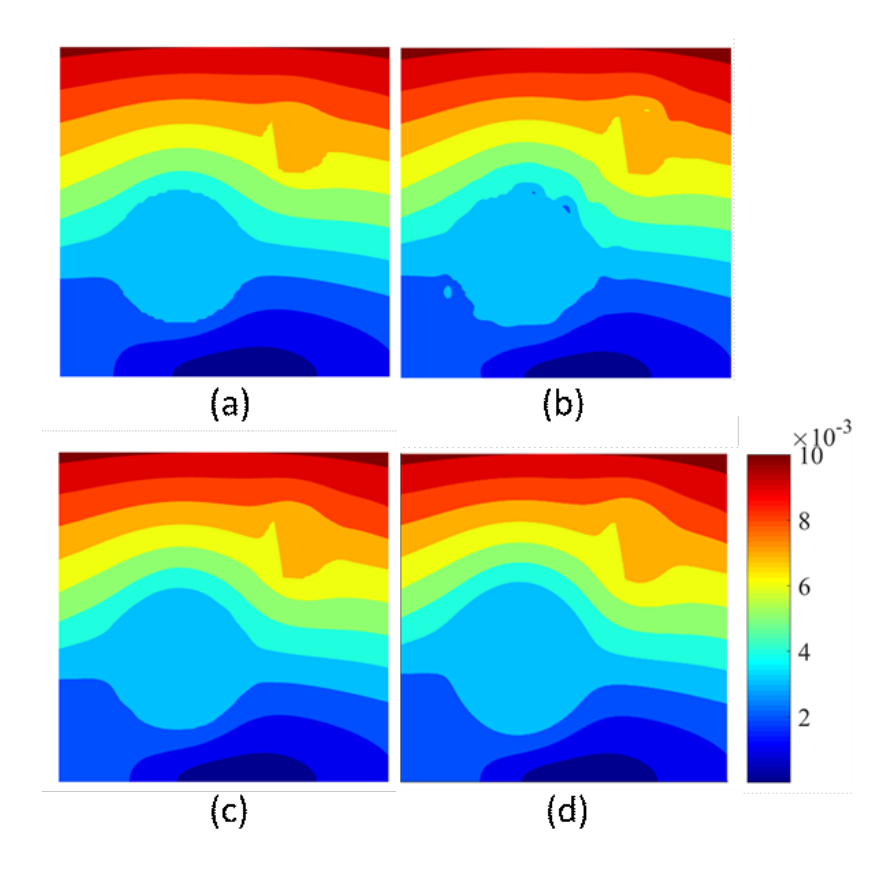


Figure 28: Contour of the effective displacement for the 2D inhomogeneous elasticity problem with $\beta=E^{(1)}$ using 549 particles: (a) penalty method; (b) Nitsche's method; (c) non-symmetric Nitsche's method; (d) reference solution by FEM.

6.4 CT scan of a composite microstructure

The last example involves segmented CT scans of a composite microstructure, shown in Figure 29, as a demonstration. 2D slices of the reconstructions are used to analyze the mechanical behavior of the composite. The matrix is polymer epoxy (EPO-TEK 203, Epoxy Technology Inc., Billerica, MA) with Young's modulus E=3.2Gpa and Poisson's' ratio $\nu=0.4$. The inclusions in the matrix are Alumina (Saint-Gobain, Malvern, PA) with a very different Young's modulus of E=380Gpa, and Poisson's ratio $\nu=0.3$. Two meshfree discretizations of 2D slices of the segmented micro-CT are shown in Figure 30(a) and Figure 31(a), where again a mesh is shown for visualization of the domains. A roller boundary condition is applied at the bottom of the models, with a pin support at the center. A prescribed displacement corresponding to 10% tensile engineering strain is applied to the top of the model. The non-symmetric Nitsche method is selected for analysis based on the previous results.

The displacement magnitude and stress contours shown in Figures 30(b-c) and Figures 31(b-c), respectively, exhibit the inhomogeneous response of composite solids: the displacement contours deviate from the linear distribution expected from homogeneous material, and stress concentrations can be observed along the interface of inclusions, particularly around rough geometry. Some other interesting features can be observed, such as much higher stress magnitudes on the top right of Figure 30(c), and a force chain-like response in 31(c) with tensile stresses above average continuously distributed down a line of inclusions near the middle-right.

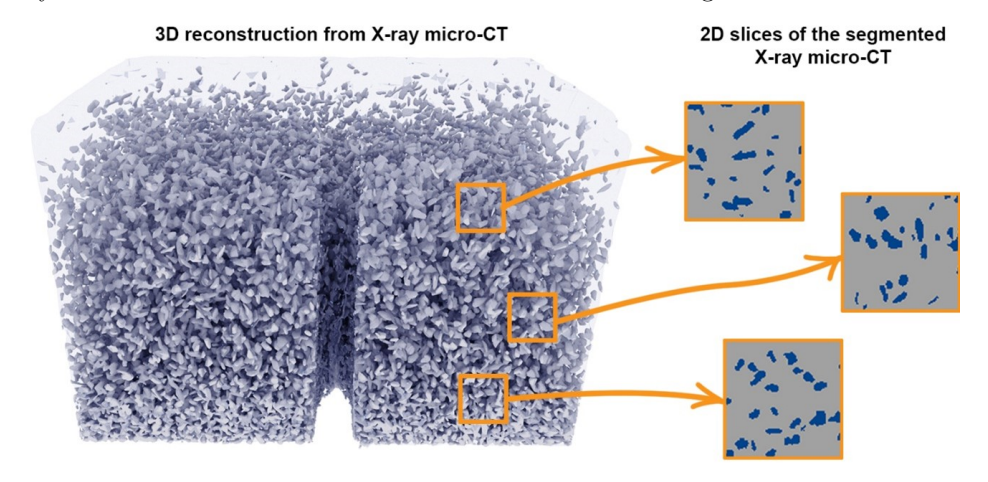


Figure 29: Problem description of CT scanned composite.

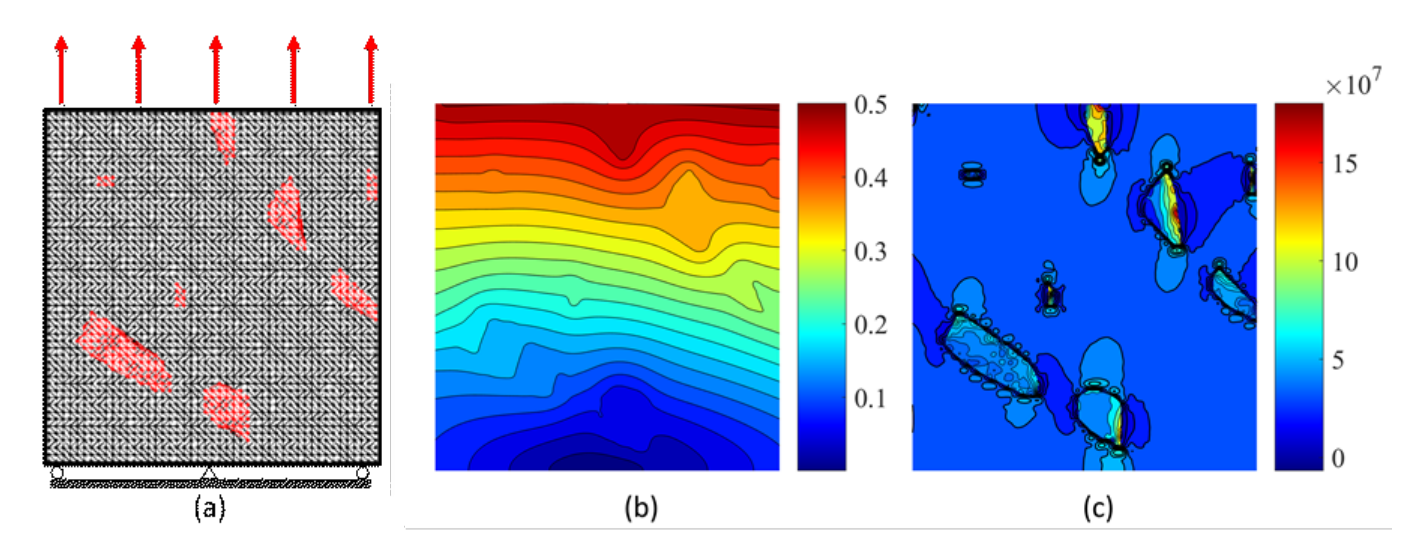


Figure 30: Meshfree simulation of CT scanned model with 2576 particles: (a) problem description and meshfree discretization; (b) displacement magnitude; (c) σ_{vv} .

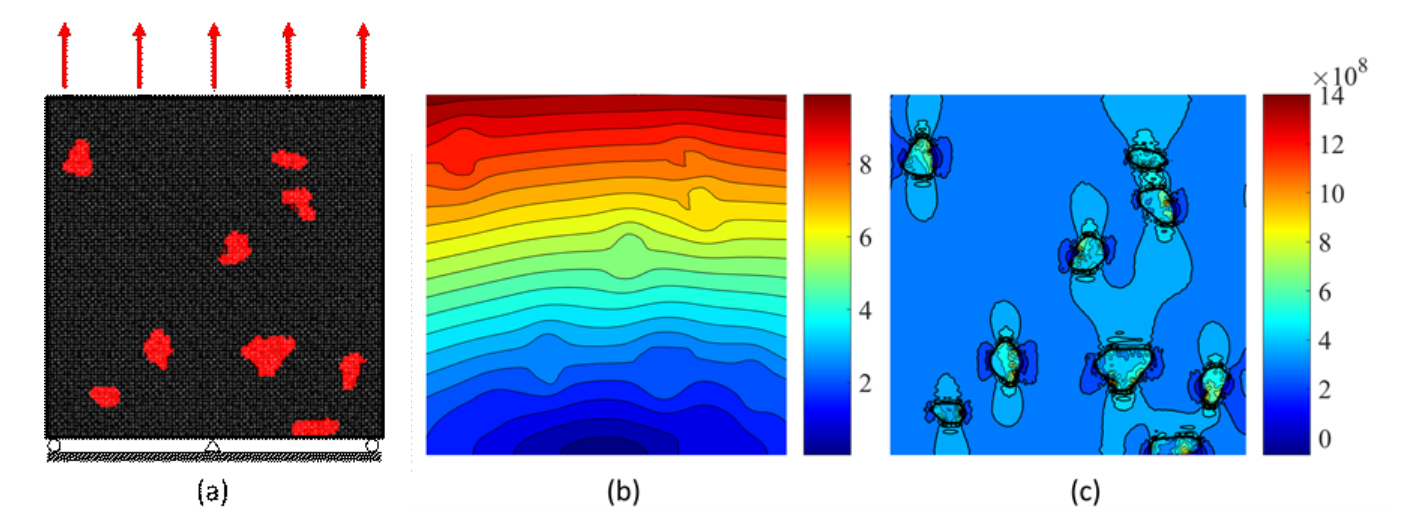


Figure 31: Meshfree simulation of CT scanned model with 10,592 particles: (a) problem description and meshfree discretization; (b) displacement magnitude; (c) σ_{vv} .

7 Conclusions and discussion

In this work, consistent immersed volumetric Nitsche (CIVN) methods are developed by using the Nitsche approach to enforce a volumetric continuity condition between the computational composite domains. The methods do not require additional degrees of freedom, and the numerical simulations will not suffer from the LBB instability condition, in contrast to the Lagrange multiplier method. The immersed volumetric Nitsche's methods are shown to be fully consistent with strong form. Due to the regularity of test and trial functions, these volumetric-type constraint approaches remain consistent with the surface constraints in the original strong form of the composite problem.

By using the immersed volumetric approach, no contour integral at the interfaces is required nor computation of cell intersections, which avoids computational complexity, the need for conforming meshes, and enables relatively effortless analysis of composite problems with arbitrarily complicated geometry. The effectiveness of the proposed CIVNs are demonstrated with several numerical examples, including real geometries of composite microstructures.

Consistent with earlier findings, Nitsche methods in the present context deliver more accurate results and exhibit much less sensitivity to the choice of the penalty parameter. This makes the Nitsche approach more robust for practical applications. In addition, when using the Nitsche technique, there is no need to select large values of the penalty parameter to obtain accurate results, which improves conditioning of the left-hand-side matrices in implicit calculations and increases the stable time-step size in explicit calculations.

A surprising finding of this work is that the non-symmetric Nitsche technique showed better accuracy and robustness than it's symmetric counterpart. Symmetric Nitsche techniques, which require higher values of the penalty parameter for stability than their non-symmetric counterparts, are nevertheless favored for more traditional applications (e.g., weak enforcement of essential boundary conditions for elliptic problems) because they preserve symmetry of the system matrix and are adjoint-consistent, leading to optimal convergence in lower-order norms. In the present case, however, adjoint consistency does not play an obvious role, and the non-symmetric Nitsche technique clearly benefits from the additional stability brought about by the skew-symmetric form of the operator. In addition, the symmetric Nitsche in this context does not lead to a symmetric system matrix anyway.

The proposed CIVN framework requires C^1 continuity of the background, but only C^0 continuity of the foreground. In this work, meshfree approximations were utilized to satisfy these conditions. However, methods such as isogemetric analysis (IGA) can also be utilized to satisfy the smoothness criteria. Thus, several combinations of methods are possible for background-foreground discretizations, for instance: IGA-IGA, IGA-meshfree, IGA-FEM, meshfree-FEM, etc.

A limitation of this method is the smoothness of the numerical solution; inherently, a smooth approximation is required, and meanwhile the true solution in composite problems will not possess sufficient regularity to obtain the standard optimal convergence rate. However, great flexibility is gained by this approach, and the solutions are nonetheless convergent.

In future work, the CIVN approach will be applied to fluid-structure interaction problems involving material failure, where the problem of parameterizing contours is severely compounded by continuously evolving topological changes of the immersed solid domain.

Acknowledgements This work was supported by the National Science Foundation award number 1826221 and the U.S. Army Engineering Research and Development Center through Ordnance Technology Initiative Agreement DOTC-17-01-INIT0880. Proofing of this manuscript by Jennifer Dougal is also acknowledged and appreciated.

Appendix

In this appendix, the proposed weak forms are derived from a weighted residual point of view. A weighted residual form of Eqs. (1a)-(1e) can be stated as:

$$R = \int_{\Omega_{B} \backslash \Omega_{F}} \boldsymbol{w}_{B} \cdot (\nabla \cdot \boldsymbol{\sigma}_{B} + \boldsymbol{b}_{B}) d\Omega - \int_{\Gamma_{t}} \boldsymbol{w}_{B} \cdot (\boldsymbol{n} \cdot \boldsymbol{\sigma}_{B} - \bar{\boldsymbol{t}}) d\Gamma$$

$$+ \int_{\Omega_{F}} \boldsymbol{w}_{F} \cdot (\nabla \cdot \boldsymbol{\sigma}_{F} + \boldsymbol{b}_{F}) d\Omega - \int_{\Gamma_{I}} \boldsymbol{w}_{F} \cdot [\boldsymbol{n}_{I} \cdot (\boldsymbol{\sigma}_{F} - \boldsymbol{\sigma}_{B})] d\Gamma$$

$$= 0. \tag{44}$$

After integration by parts, we arrive at the following weak form:

$$R = \int_{\Omega_{B} \backslash \Omega_{F}} \nabla^{s} \boldsymbol{w}_{B} : \boldsymbol{\sigma}_{B} d\Omega - \int_{\Omega_{B} \backslash \Omega_{F}} \boldsymbol{w}_{B} \cdot \boldsymbol{b}_{B} d\Omega - \int_{\Gamma_{t}} \boldsymbol{w}_{B} \cdot \bar{\boldsymbol{t}} d\Gamma$$

$$+ \int_{\Omega_{F}} \nabla^{s} \boldsymbol{w}_{F} : \boldsymbol{\sigma}_{F} d\Omega - \int_{\Omega_{F}} \boldsymbol{w}_{F} \cdot \boldsymbol{b}_{F} d\Omega - \int_{\Gamma_{I}} (\boldsymbol{w}_{F} - \boldsymbol{w}_{B}) \cdot (\boldsymbol{n}_{I} \cdot \boldsymbol{\sigma}_{B}) d\Gamma$$

$$= 0. \tag{45}$$

From Eq. (45), one can see that this formulation still contains a contour integral on the interface. To eliminate this term, first define the following:

$$R^{(1)} = \int_{\Omega_F} \nabla^s \boldsymbol{w}_B : \boldsymbol{\sigma}_B - \boldsymbol{w}_B \cdot \boldsymbol{b}_B d\Omega$$

$$R^{(2)} = \int_{\Omega_F} \nabla^s \boldsymbol{w}_F : \boldsymbol{\sigma}_B - \boldsymbol{w}_F \cdot \boldsymbol{b}_B d\Omega.$$
(46)

Next, we modify Eq. (45) by adding and subtracting the terms in (91):

$$0 = R + (R^{(1)} - R^{(1)}) + (R^{(2)} - R^{(2)})$$

$$= \int_{\Omega_B} \nabla^s \boldsymbol{w}_B : \boldsymbol{\sigma}_B - \boldsymbol{w}_B \cdot \boldsymbol{b}_B d\Omega - \int_{\Gamma_t} \boldsymbol{w}_B \cdot \bar{\boldsymbol{t}} d\Gamma$$

$$+ \int_{\Omega_F} \nabla^s \boldsymbol{w}_F : (\boldsymbol{\sigma}_F - \boldsymbol{\sigma}_B) - \boldsymbol{w}_F \cdot (\boldsymbol{b}_F - \boldsymbol{b}_B) d\Omega - \int_{\Gamma_I} (\boldsymbol{w}_F - \boldsymbol{w}_B) \cdot (\boldsymbol{n}_I \cdot \boldsymbol{\sigma}_B) d\Gamma$$

$$- \int_{\Omega_F} \nabla^s \boldsymbol{w}_B : \boldsymbol{\sigma}_B - \boldsymbol{w}_B \cdot \boldsymbol{b}_B d\Omega + \int_{\Omega_F} \nabla^s \boldsymbol{w}_F : \boldsymbol{\sigma}_B - \boldsymbol{w}_F \cdot \boldsymbol{b}_B d\Omega.$$

$$(47)$$

An integration by parts on Eq. (47) directly eliminates the boundary integral:

$$0 = \int_{\Omega_B} \nabla^s \boldsymbol{w}_B : \boldsymbol{\sigma}_B - \boldsymbol{w}_B \cdot \boldsymbol{b}_B d\Omega - \int_{\Gamma_t} \boldsymbol{w}_B \cdot \bar{\boldsymbol{t}} d\Gamma$$

$$+ \int_{\Omega_F} \nabla^s \boldsymbol{w}_F : (\boldsymbol{\sigma}_F - \boldsymbol{\sigma}_B) - \boldsymbol{w}_F \cdot (\boldsymbol{b}_F - \boldsymbol{b}_B) d\Omega$$

$$- \int_{\Omega_F} (\boldsymbol{w}_F - \boldsymbol{w}_B) \cdot (\nabla \cdot \boldsymbol{\sigma}_B + \boldsymbol{b}_B) d\Omega.$$
(48)

From the derivation, the above weak form attests to Eqs. (1a)–(1e), yet the compatibility condition (1f) still needs to be enforced.

Now, instead of enforcing compatibility on interface (1f), consider the following augmented weighted residual form by enforcing $u_B = u_F$ on Ω_F :

$$\bar{R} = R + \int_{\Omega_F} \boldsymbol{w} \cdot (\boldsymbol{u}_F - \boldsymbol{u}_B) d\Omega = 0$$
(49)

in which a new test function is introduced. Usually, the selection of \boldsymbol{w} should be arbitrary. Nevertheless, since it is defined in Ω_F , \boldsymbol{w} cannot be directly related to \boldsymbol{u}_F . Now, in order to derive the CIVNs from Eq. (49), one can select \boldsymbol{w} as follows:

$$\mathbf{w} = \begin{cases} -\nabla \cdot \boldsymbol{\sigma}(\mathbf{w}_B) & \text{for Nitsche} \\ \nabla \cdot \boldsymbol{\sigma}(\mathbf{w}_B) & \text{for non - symmetric Nitsche} \end{cases}$$
 (50)

Finally, the volumetric immersed formulation is obtained from Eqs (48)-(50), with the addition of a penalty term:

$$\int_{\Omega_{B}} \nabla^{s} \boldsymbol{w}_{B} : \boldsymbol{\sigma}_{B} d\Omega - \int_{\Omega_{B}} \boldsymbol{w}_{B} \cdot \boldsymbol{b}_{B} d\Omega + \int_{\Omega_{F}} \nabla^{s} \boldsymbol{w}_{F} : (\boldsymbol{\sigma}_{F} - \boldsymbol{\sigma}_{B}) d\Omega
- \int_{\Omega_{F}} \boldsymbol{w}_{F} \cdot (\boldsymbol{b}_{F} - \boldsymbol{b}_{B}) d\Omega - \int_{\Gamma_{t}} \boldsymbol{w}_{B} \cdot \bar{\boldsymbol{t}} d\Gamma - \int_{\Omega_{F}} \nabla \cdot \boldsymbol{\sigma}(\boldsymbol{w}_{B}) \cdot (\boldsymbol{u}_{F} - \boldsymbol{u}_{B}) d\Omega
- \int_{\Omega_{F}} (\boldsymbol{w}_{F} - \boldsymbol{w}_{B}) \cdot (\nabla \cdot \boldsymbol{\sigma}_{B} + \boldsymbol{b}_{B}) d\Omega + \beta \int_{\Omega_{F}} (\boldsymbol{w}_{B} - \boldsymbol{w}_{F}) \cdot (\boldsymbol{u}_{B} - \boldsymbol{u}_{F}) d\Omega = 0$$
(51)

which is the same as the proposed formulation in Eq. (17). The derivation for the non-symmetric version follows directly. Thus, although the proposed method cannot be obtained from a variational viewpoint, it can still be grounded in the weighted residual formulation.

One final comment, consider the variational derivative of the Lagrange multiplier to enforce volumetric compatibility:

$$\delta \left[(\boldsymbol{u}_F - \boldsymbol{u}_B) \cdot \boldsymbol{\lambda} \right] = (\delta \boldsymbol{u}_F - \delta \boldsymbol{u}_B) \cdot \boldsymbol{\lambda} + \delta \boldsymbol{\lambda} \cdot (\boldsymbol{u}_F - \boldsymbol{u}_B). \tag{52}$$

Likewise, the terms in weak form (51) can be thought of as emanating from the following variational derivative:

$$\delta \left[(\boldsymbol{u}_F - \boldsymbol{u}_B) \cdot (\nabla \cdot \boldsymbol{\sigma}_B + \boldsymbol{b}_B) \right] = (\delta \boldsymbol{u}_F - \delta \boldsymbol{u}_B) \cdot (\nabla \cdot \boldsymbol{\sigma}_B + \boldsymbol{b}_B) + \nabla \cdot \delta \boldsymbol{\sigma}_B \cdot (\boldsymbol{u}_F - \boldsymbol{u}_B). \tag{53}$$

Comparing Eqs. (52) and (53), it is apparent that one has by analogy:

$$\lambda = \nabla \cdot \boldsymbol{\sigma}_B + \boldsymbol{b}_B. \tag{54}$$

Which also indicates that the constraint terms in the weak form (51) is equivalent to using the physical meaning of the Lagrange multiplier to enforce the constraint. Finally, in a variational form, (51) with the aid of (54) can be rewritten as follows:

$$\int_{\Omega_{B}} \nabla^{s} \delta \boldsymbol{u}_{B} : \boldsymbol{\sigma}_{B} d\Omega - \int_{\Omega_{B}} \delta \boldsymbol{u}_{B} \cdot \boldsymbol{b}_{B} d\Omega + \int_{\Omega_{F}} \nabla^{s} \delta \boldsymbol{u}_{F} : (\boldsymbol{\sigma}_{F} - \boldsymbol{\sigma}_{B}) d\Omega - \int_{\Omega_{F}} \delta \boldsymbol{u}_{F} \cdot (\boldsymbol{b}_{F} - \boldsymbol{b}_{B}) d\Omega
- \int_{\Gamma_{I}} \delta \boldsymbol{u}_{B} \cdot \bar{\boldsymbol{t}} d\Gamma + \int_{\Omega_{F}} \delta \boldsymbol{\lambda} \cdot (\boldsymbol{u}_{F} - \boldsymbol{u}_{B}) d\Omega + \int_{\Omega_{F}} (\delta \boldsymbol{u}_{F} - \delta \boldsymbol{u}_{B}) \cdot \boldsymbol{\lambda} d\Omega = 0$$
(55)

which is identical to the form in [33], and demonstrates that the method can be grounded in weighted residual principles.

References

- [1] R. Glowinski, T.-W. Pan, J. Periaux, A fictitious domain method for dirichlet problem and applications, Computer Methods in Applied Mechanics and Engineering 111 (3-4) (1994) 283–303.
- [2] F. P. Baaijens, A fictitious domain/mortar element method for fluid–structure interaction, International Journal for Numerical Methods in Fluids 35 (7) (2001) 743–761.
- [3] P. Hansbo, C. Lovadina, I. Perugia, G. Sangalli, A Lagrange multiplier method for the finite element solution of elliptic interface problems using non-matching meshes, Numerische Mathematik 100 (1) (2005) 91–115.
- [4] E. Burman, P. Hansbo, Interior-penalty-stabilized lagrange multiplier methods for the finite-element solution of elliptic interface problems, IMA Journal of Numerical Analysis 30 (3) (2010) 870–885.
- [5] J. Nitsche, Über ein variationsprinzip zur lösung von dirichlet-problemen bei verwendung von teilräumen, die keinen randbedingungen unterworfen sind, in: Abhandlungen aus dem mathematischen Seminar der Universität Hamburg, Vol. 36, Springer, 1971, pp. 9–15.
- [6] A. Hansbo, P. Hansbo, An unfitted finite element method, based on Nitsche's method, for elliptic interface problems, Computer Methods in Applied Mechanics and Engineering 191 (47-48) (2002) 5537–5552.

- [7] P. Hansbo, Nitsche's method for interface problems in computational mechanics, GAMM-Mitteilungen 28 (2) (2005) 183–206.
- [8] C. Annavarapu, M. Hautefeuille, J. E. Dolbow, A robust Nitsche's formulation for interface problems, Computer Methods in Applied Mechanics and Engineering 225 (2012) 44–54.
- [9] C. Annavarapu, M. Hautefeuille, J. E. Dolbow, A Nitsche stabilized finite element method for frictional sliding on embedded interfaces. part I: Single interface, Computer Methods in Applied Mechanics and Engineering 268 (2014) 417–436.
- [10] C. Annavarapu, M. Hautefeuille, J. E. Dolbow, A Nitsche stabilized finite element method for frictional sliding on embedded interfaces. part II: Intersecting interfaces, Computer Methods in Applied Mechanics and Engineering 267 (2013) 318–341.
- [11] J. D. Sanders, T. A. Laursen, M. A. Puso, A Nitsche embedded mesh method, Computational Mechanics 49 (2) (2012) 243–257.
- [12] Z. Li, T. Lin, X. Wu, New Cartesian grid methods for interface problems using the finite element formulation, Numerische Mathematik 96 (1) (2003) 61–98.
- [13] J. D. Sanders, J. E. Dolbow, T. A. Laursen, On methods for stabilizing constraints over enriched interfaces in elasticity, International Journal for Numerical Methods in Engineering 78 (9) (2009) 1009–1036.
- [14] E. Burman, Ghost penalty, Comptes Rendus Mathematique 348 (21-22) (2010) 1217-1220.
- [15] T. Strouboulis, K. Copps, I. Babuška, The generalized finite element method, Computer Methods in Applied Mechanics and Engineering 190 (32-33) (2001) 4081–4193.
- [16] T. Strouboulis, I. Babuška, K. Copps, The design and analysis of the generalized finite element method, Computer Methods in Applied Mechanics and Engineering 181 (1-3) (2000) 43–69.
- [17] J. Melenk, I. Babuška, The partition of unity finite element method: Basic theory and applications, Computer Methods in Applied Mechanics and Engineering 139 (1-4) (1996) 289–314.
- [18] N. Moës, J. Dolbow, T. Belytschko, A finite element method for crack growth without remeshing, International Journal for Numerical Methods in Engineering 46 (1) (1999) 131–150.
- [19] N. Sukumar, N. Moës, B. Moran, T. Belytschko, Extended finite element method for three-dimensional crack modelling, International Journal for Numerical Methods in Engineering 48 (11) (2000) 1549–1570.
- [20] T. Belytschko, N. Moës, S. Usui, C. Parimi, Arbitrary discontinuities in finite elements, International Journal for Numerical Methods in Engineering 50 (4) (2001) 993–1013.
- [21] T.-P. Fries, T. Belytschko, The extended/generalized finite element method: an overview of the method and its applications, International journal for numerical methods in engineering 84 (3) (2010) 253–304.
- [22] P. Laborde, J. Pommier, Y. Renard, M. Salaün, High-order extended finite element method for cracked domains, International Journal for Numerical Methods in Engineering 64 (3) (2005) 354–381.
- [23] T.-P. Fries, A. Zilian, On time integration in the XFEM, International Journal for Numerical Methods in Engineering 79 (1) (2009) 69–93.
- [24] K. Park, J. P. Pereira, C. A. Duarte, G. H. Paulino, Integration of singular enrichment functions in the generalized/extended finite element method for three-dimensional problems, International Journal for Numerical Methods in Engineering 78 (10) (2009) 1220–1257.
- [25] J. Chessa, H. Wang, T. Belytschko, On the construction of blending elements for local partition of unity enriched finite elements, International Journal for Numerical Methods in Engineering 57 (7) (2003) 1015–1038.
- [26] C. S. Peskin, Numerical analysis of blood flow in the heart, Journal of computational physics 25 (3) (1977) 220–252.
- [27] C. S. Peskin, The immersed boundary method, Acta Numerica 11 (2002) 479–517.
- [28] L. Zhang, A. Gerstenberger, X. Wang, W. K. Liu, Immersed finite element method, Computer Methods in Applied Mechanics and Engineering 193 (21-22) (2004) 2051–2067.

- [29] X. Wang, L. T. Zhang, Modified immersed finite element method for fully-coupled fluid–structure interactions, Computer Methods in Applied Mechanics and Engineering 267 (2013) 150–169.
- [30] W. K. Liu, D. W. Kim, S. Tang, Mathematical foundations of the immersed finite element method, Computational Mechanics 39 (3) (2007) 211–222.
- [31] H. Wang, J. Chessa, W. K. Liu, T. Belytschko, The immersed/fictitious element method for fluid–structure interaction: volumetric consistency, compressibility and thin members, International Journal for Numerical Methods in Engineering 74 (1) (2008) 32–55.
- [32] C. Wu, Y. Guo, E. Askari, Numerical modeling of composite solids using an immersed meshfree galerkin method, Composites Part B: Engineering 45 (1) (2013) 1397–1413.
- [33] P. Blanco, R. Feijóo, E. Dari, A variational framework for fluid-solid interaction problems based on immersed domains: theoretical bases, Computer Methods in Applied Mechanics and Engineering 197 (25-28) (2008) 2353– 2371.
- [34] H. B. Dhia, Multiscale mechanical problems: the arlequin method, Comptes Rendus de l'Academie des Sciences Series IIB Mechanics Physics Astronomy 12 (326) (1998) 899–904.
- [35] H. B. Dhia, G. Rateau, Analyse mathématique de la méthode arlequin mixte, Comptes Rendus de l'Académie des Sciences-Series I-Mathematics 332 (7) (2001) 649–654.
- [36] J. W. D. Fernandes, A. Barbarulo, H. B. Dhia, R. A. K. Sanches, A residual-based stabilized finite element formulation for incompressible flow problems in the arlequin framework, Computer Methods in Applied Mechanics and Engineering 370 (2020) 113073.
- [37] H. B. Dhia, G. Rateau, The arlequin method as a flexible engineering design tool, International journal for numerical methods in engineering 62 (11) (2005) 1442–1462.
- [38] L. H. Nguyen, S. K. Stoter, M. Ruess, M. A. Sanchez Uribe, D. Schillinger, The diffuse nitsche method: Dirichlet constraints on phase-field boundaries, International Journal for Numerical Methods in Engineering 113 (4) (2018) 601–633.
- [39] J.-S. Chen, M. Hillman, S.-W. Chi, Meshfree methods: progress made after 20 years, Journal of Engineering Mechanics 143 (4) (2017) 04017001.
- [40] J. A. Cottrell, T. J. Hughes, Y. Bazilevs, Isogeometric analysis: toward integration of CAD and FEA, John Wiley & Sons, 2009.
- [41] S. Fernández-Méndez, A. Huerta, Imposing essential boundary conditions in mesh-free methods, Computer Methods in Applied Mechanics and Engineering 193 (12-14) (2004) 1257–1275.
- [42] W. K. Liu, S. Jun, Y. F. Zhang, Reproducing kernel particle methods, International journal for numerical methods in fluids 20 (8-9) (1995) 1081–1106.
- [43] H. Zhang, D. Wang, An isogeometric enriched quasi-convex meshfree formulation with application to material interface modeling, Engineering Analysis with Boundary Elements 60 (2015) 37–50.
- [44] M. Griebel, M. A. Schweitzer, A particle-partition of unity method part V: boundary conditions, in: Geometric analysis and nonlinear partial differential equations, Springer, 2003, pp. 519–542.
- [45] E. Burman, A penalty-free nonsymmetric nitsche-type method for the weak imposition of boundary conditions, SIAM Journal on Numerical Analysis 50 (4) (2012) 1959–1981.